Integration of GIS, Laboratory and Magnetic Field Data Interpretation for Identification of Laterite Beds in Eastern Salt Range, Pakistan.

By

Shahzaib Sheikh (02112011003)

M.PHIL. (GEOPHYSICS)

2020-2022

DEPARTMENT OF EARTH SCIENCES
QUAID-I- AZAM UNIVERSITY

CERTIFICATE OF APPROVAL

This dissertation submitted by **SHAHZAIB SHEIKH** S/O **SHEIKH FAYYAZ AHMED** is accepted in its present form by the Department of Earth Sciences, Quaid-I-Azam University Islamabad as satisfying the requirement for the award of degree of **M.Phil Geophysics.**

RECOMMENDED BY

Dr. Aamir Ali
(Chairman/ Supervisor) _____

External Examiner _____

ACKNOLEDGEMENT

In the name of **Allah**, the most Beneficent, the most Merciful. All praises to **Almighty Allah**, the creator of universe. Secondly, my humblest gratitude to the **Holy Prophet Muhammad (Peace Be Upon Him)**. Without the blessing of Allah, I could not be able to complete my work as well as to be at such a place. This thesis appears in its current form due to the assistance and guidance of several people. It gives me great pleasure to express my gratitude to all those who supported me and have contributed to making this thesis possible.

I express my profound sense of reverence to **Dr. Aamir Ali Associate Professor**, who gave me the opportunity to work under his supervision on such outstanding research. His continuous support, motivation and untiring guidance have made this thesis possible. His vast knowledge, calm nature and positive criticism motivated me to push harder to get the best forms of results. I thank him for bearing my mistakes and being the "teacher" that many fails to understand the true concept of this elevated post bestowed upon them.

Also, I am immensely pleased to place on record my deep gratitude and heartfelt thanks to **Umer Farooq** and **Yawar Amin** who helped me throughout this research period, and my friends and many others without whom this course work would have been hard to be completed.

Last but not the least, I would like to acknowledge my family for their constant support, unceasing prayers and best wishes. My parents specially to whom I thank the most who helped me most with their constant support throughout the time for the successful completion of my thesis. Those missed to be named are always close to my heart, and if not named in the acknowledgment are fully thanked.

SHAHZAIB SHEIKH
M.Phil. GEOPHYSICS
2020-2022

Contents

List of Figures

List of Tables

ABSTRACT

The modern world prioritizes sustainable, environment friendly energy resources making mineral exploration a key factor for construction and development. Minerals play an imperative role in economic development as well as technological advancement of any country. With exploration focused primarily on hydrocarbon industry, mineral exploration of rare or industrial minerals has been largely an ignored topic in Pakistan. The objective of this study is to investigate the subsurface presence of regional features associated to the industrial laterite mineral, an eco-friendlier construction material, in economic quantity in the Eastern Salt Range of Pakistan. The methodology adopted for this study involves the geochemical analysis of samples obtained during geological field and remote sensing techniques of Principal Component Analysis (PCA), band rationing (BR), and advanced mineral mapping to validate the regional exposures in the area. Furthermore, the results have been integrated with magnetic data acquired in the vicinity of the villages Ratuchah and Pidh at final stage. Geochemical analysis of samples showed large percentage of quartz mineral with iron oxide as the second most abundant mineral. PCA provided clear segregation of the laterite beds, sand bodies, carbonates, and clay content present in the area. The PCA band combination of 7, 5, 4 was able to visualize the presence of left lateral strike fault in the subsurface. Band rationing combined with advanced mineral mapping helped in pinpointing the presence of iron oxides in laterite beds with a 98% confidence level. Furthermore, the magnetic data interpretation confirmed the presence of left lateral strike slip fault trending northeast to southwest. Reduction to Pole (RTP) mapped much smoother anomalies in contrast to the residual total magnetic intensity map. First vertical derivative enhanced the short wavelength anomalies caused by the ferromagnetic laterite beds and application of tilt derivative further resolved the extension of laterite beds confirming their presence towards the southwest region. Although the results obtained were feasible in achieving the objectives, however a more detailed study of the region with aeromagnetic data and additional geological samples for lab analysis involving XRF can be combined to further validate potential of the study area.

CHAPTER 01

INTRODUCTION

1.1 Introduction

Pakistan is endowed with a diverse range of minerals oscillating from valuable metals to numerous gemstones with a vast content of industrial minerals such as barite, marble, talc, halite, and coal. Even though so many potential mineral zones have been indicated, there are still many places left undiscovered in terms of these minerals. Minerals are essential for each nation's economic growth and development, yet understanding regarding the mineralogical composition, occurrence, and reserves available on surface and subsurface of many minerals is limited (Ajaka and Oyathelemi, 2010). Our modern society needs huge quantities of mineral resources that can be extracted from the lithosphere of the earth's crust. The term mining refers to exploration and extraction as well as production and processing of these treasures obtained from the ground (EUMICON, 2018). Mining operations provide most raw chemicals and substances for material used at home and in industry (Vogley, 1985). Laterite soil has clay minerals that are particularly high in illite and montmorillonite concentration (Portelinha et al., 2012), hence the possibility for damage is larger if construction activity is done on such soils. Because clay minerals and metals are abundant, they has been used for a vast variety of purposes such as cement making, road construction, and other applications. However, before its usage, the soil's properties and the possibilities of restoration must be studied.

Laterite soil is a soil group created by the accumulation of hydrated hematite and aluminium because of extremely high weathering (Thagesen, 1996). If dry circumstances persist, this type of soil adopts rigid, impenetrable, and difficult to modify features (Makasa, 2004). Laterite has a wide colour range from red to yellow to brown, fine texture, a nodular shape, and is firmly cemented (Saing et al., 2017). Numerous authors have written about the benefits of laterite in terms of its use as compressed earth brick (CEB), with some of the most noteworthy works being Houben and Guillaud, 1994; Rigassi, 1995; Adam and Agib, 2001; Kasthurba et al., 2007; Al-Jabri and Shoukry, 2014; Oyelami and Van Rooy, 2016. These case studies promote the importance of CEBs toward the environment. CEBs are defined as substances for sustainable building construction that promote environmental sustainability. Building in a 'sustainable' manner allows us to use our resources more efficiently without compromising public health quality and well-being as well as

to effectively conserve a better environment. When used properly, earth materials do not result in the same level of resource exhaustion, wastage and pollution, or biological changes as conventional building materials (Bachar et al., 2015).

Contemporary investigation for delineation of deposits involves conventional strategies such as geological mapping in consolidation with modern techniques developed through the disciplines of geochemistry and geophysics alongside satellite imagery. The ongoing idea in this multitude of techniques is the identification of unobtrusive differences in the actual properties of earth materials, which might give evident fingerprints of significant minerals (Coates, 1985). Geochemical prospecting deals with careful inspection of soil, rock, and vegetation contrast in order to detect any abnormalities which may hint towards the presence of a metalliferous deposit. The presence of distinctive radiating` substances found in soil could act as a metal indicator in the subsurface. Presence of certain gases such as helium and sulfur or elements such as mercury indicate probable existence of substantial metals underground. Geophysical investigations make use tools that detect a physical property such as density, electrical conductivity, magnetism etc. to analyze the earth layers with regards to the objective. The acquired information is examined relative to predefined principles, thus confirming the potential of extractable assets (Coates, 1985).

Investigation in rugged terrain has become fairly easy with the rise in satellite data analysis for identification of rock types and enhanced spectral signatures that can be matched with field samples. In one such inquiry in the Nigerian region of Orin Ekiti, the shuttle radar topographic mission digital elevation model was interpreted to identify favourable features in context to the bauxite occurrence in the study area (Talabi et al., 2018). The bauxite occurrences attributed to conditions such as settlement, altitude, slope, rocks, and vegetation occurring at a height of 710 meters, generally considered as a low sloping region (Talabi et al., 2018; Amosun et al., 2020). This was then combined with the use of aeromagnetic data which indicated changes in magnetic field intensity across the study area due to variations in mineral content inside distinct lithologies and depths of the rocks (Amosun et al., 2020). The area under study on which remote sensing data was utilized to mark the bauxite appearances on a reconnaissance scale was further subdivided into three magnetic zones with the low susceptibility range between -938.1 nT to 48.0 nT, medium zone range of 48.0 nT to 99.2 nT, and the high zone from 99.2 nT to 460.7 nT. Further enhancement on the total magnetic intensity map (TMI) was carried out through reduction to equator (RTE) to

remove near-surface irregularities and enhancement of the anomalous magnetic signatures resulting in identification of charnockitic rocks as low magnetic zone anomalies in study area (Amosun et al., 2020). Furthermore, total horizontal derivative (THD) delineated faults and edges within the low susceptibility rocks, whereas Euler Deconvolution maps explored the depth and location of new potential magnetic anomaly based mineral sources in the study area (Amosun et al., 2020).

Satellite photography from highly elevated orbiting mechanical research facilities, such as the original Earth Resources Technology Satellite followed by its successor structure referred as LANDSAT, is extremely important for planning vast sections. The Advanced Spaceborne Thermal Emission and Reflection Radiometer (ASTER) data has relatively high spectral resolution and covers three spectral configurations in the Visible Near Infrared region (VNIR), six in the Short-Wave Infrared region (SWIR), and five in the Thermal Infrared region (TIR), thus providing a relatively detailed information in the altered zones compared to other multispectral data (Chakraborty et al., 2015). The information supplied by these sensors have been helpful in discovering encouraging novel structures suitable for mineral storage, as well as vegetation contrast estimation which is a key mineral exploration factor. Some trees, for example, have leaves susceptible to metals like nickel, copper, and zinc. Such dirt components can obstruct chlorophyll formation, which can be detected by infrared groups that work upon light intensity disparities (Coates, 1985).

A recently used technique in remote sensing includes analysis of satellite images, their processing, visual interpretation, and creation of various themed maps capable of including details of the geology and physiography of the area of interest (Amosun et al., 2020). The most common techniques applied on multispectral data for identification of laterite and bauxite beds are Band rationing (BR) and Principal Component Analysis (PCA) (Sabins, 1999). Mineral assemblages can effectively be detected using BR which improves the spectrum contrast among bands and PCA which is used for spectral enhancement. The spectral information of the scene can be represented using BR, regardless of the lighting conditions (Lilisand, 2008). The PCA technique, on the other hand, can be regarded as a statistical tool that inhibits the regulating illumination effects of the bands, therefore optimizing images by removing the correlations crucial to sensor (Crosta and Moore, 1989).

A study was conducted in the Bhukia region of Rajashan in which BR and PCA techniques were employed on the US geological survey dataset of the region where geological evidence of minerals was found (Chakraborty et al., 2015). The spectral signatures were able to demarcate ferric iron using the band ratio of 2/1, laterite through 4/5, and gossan through 4/2. The RGB composition was developed in which red color depicted ferric iron (Chakraborty et al., 2015). PCA was implemented to all the same data, but specifically to bands 1, 2, 3, and 4 of the ASTER bands, wherein the statistics file was created and evaluated. It was discovered that the fourth principal component shows the widest distribution in eigenvectors between bands 2 and 1 even with the outcomes of the ferric iron band ratio or ASTER bands 2/1. Consequently, principal component four showcased the presence of ferric iron. Eigenvector in band two had a positive loading, indicating that the bright pixels in the component image represented ferrous iron (Chakraborty et al., 2015).

Similarly, another literature review of bauxite assessment using remote sensing in the Jharkhand region of India revealed the use of PCA analysis on ASTER data as a beneficial technique in mapping (Guha et al., 2013). The PC-2 of ratio images with the identical signatures of eigenvector loading for the bauxite ratio and the eigenvector loading of the laterite index were transposed, and consequently, the PC-2 was density sliced to separate the bauxite from the laterite (Guha et al., 2013).

To carry out objectives of this study, geochemical analysis of the samples was carried out, with the ASTER dataset, with techniques namely PCA, BR, advanced mineral mapping and accuracy assessment being utilized for the interpretation of the ASTER data. The surficial results were correlated with terrestrial magnetic data that was acquired, processed, and interpreted.

1.2 Objectives

- To demarcate regional distribution of laterite and iron bearing laterite zones through remote sensing techniques.
- To gather geological samples of the laterite zones for mineral content quantification.
- Employment of magnetic data for spatial distribution analysis of laterite beds in the subsurface.
- Usage of the geophysical techniques of magnetic investigation for structural analysis of the subsurface zonation of the laterite beds.

1.3 Study Area

The area under study in this research is situated in the north-western part of the Eastern Salt Range, and in the south-eastern part of the Potowar region, where the Dil-Jabba Thrust is visible in the outcrop running in the NE to SW direction with the detailed study area lying in the vicinity of Ratuchah, of tehsil Choa Saiden Shah district Chakwal, situated 160.5km away from the capital city of Islamabad. The study area can be found between the longitude of 72° 58'E to 73° 00'E and latitude 32° 42'N to 32° 40'N, with a total area of 8.94 square kilometres lying in UTM zone 43N of datum WGS84, as shown in Figure 1.1.

1.4 Physiography

The research region is located near the Dalawal Plateau, where the Salt Range meets the Potowar Plateau., which is considered as western part of the Eastern Slat Range, with the Dil-Jabba Thrust running in the NE to SW direction in the west, and the Salt Range mountains in the east and south, bounded by an approximately east- west trending ridge which has a relief of 107 to 152 meters (m), and the well-known Dhariala Khajula anticlinal structures are part of this ridge. Elevation of the area can be averaged to 680m, with the area having rugged terrain and in most areas' outcrops of Eocene carbonates in vertical to sub vertical thrust. Structures are vivid in the north, east, west, and south, resultant of the stresses of the Himalayan Frontal Thrust, and salt tectonism playing key role for such structures. The drainage of the Dalwal plateau cuts through the ridges towards the north and empties in the Bunhar river toward Chakwal in the Potwar Plateau, with the climate of the area being arid to semi-arid.

1.5 Methodology

Approach to this study was conducted with careful planning and analysis of the literature analysis of the study area, with the elevation checked through toposheets 43-D/14, 43-H/1, and 43-H/2, with the accessibility of the location checked through Google Earth Pro. Previous work done in nearby areas of the study area was studied through the Geological Survey of Pakistan (GSP) Information record 237 of the lateritic exposures of the surrounding area. Furthermore, the geological exposure was mapped out using remote sensing software ENVI 5.3 which mapped out the mineral reflectance of laterite and associated ferric minerals which constituted majorly in the exposed zones of the lateritic beds. After which the most accessible ground location was identified in between the villages of Ratuchah and Dandot selected for ground data acquisition of magnetic data using Geometrics G-856 proton precision magnetometer with a 100m x 100m grid was

designed which became the base map of the data acquisition using ArcMap 10.4, in UTM projection 43N of datum WGS84. The total profile length was selected up to 2.5km in length and extended towards the southeast till Pidh where a total of 325 data points, i.e., 20 profiles were covered with the help of Magellan Triton handheld GPS, for detailed imaging of the lateritic beds in the subsurface and structural features associated with the Salt Range Thrust, and the Dil-Jabba thrust.

The organisation of the study is with the detailed analysis of the tectonic and stratigraphic that has been done in the second chapter, with the use of previous literature and on field analysis of the data, where samples were calculated and then tested in the laboratory with geochemical analysis confirming the presence of altered zone containing ferric minerals in high quantity, making it a feasible economic deposit. The third chapter utilizes the application of remote sensing in modern research and talks about the detailed classification and mapping of the minerals with the help of satellite data's electromagnetic bands, and how the reconnaissance of the study area was done in mapping the mineral bodies, that were too difficult to approach on foot, and became the foundation of identifying the location of the geophysical investigation to be carried out.

Fourth chapter talks on the need of applying geophysical investigative techniques in the field of mining and mineral exploration, that with the foundation laid out by geological work, and mapping the minerals using remote sensing on the surface exposures is not enough, but in fact subsurface extension of the bodies need to be mapped out for effective economic exploitation of the mineral deposits, it further goes on to image the results obtained by ground data acquisition and their further mapping in the subsurface of where the deposits are present. With the final chapter fully analysing and discussing the results of the integrated technique of remote sensing, laboratory and geophysical investigation and laying out the results obtained as a conclusion of the study, with further recommendations.

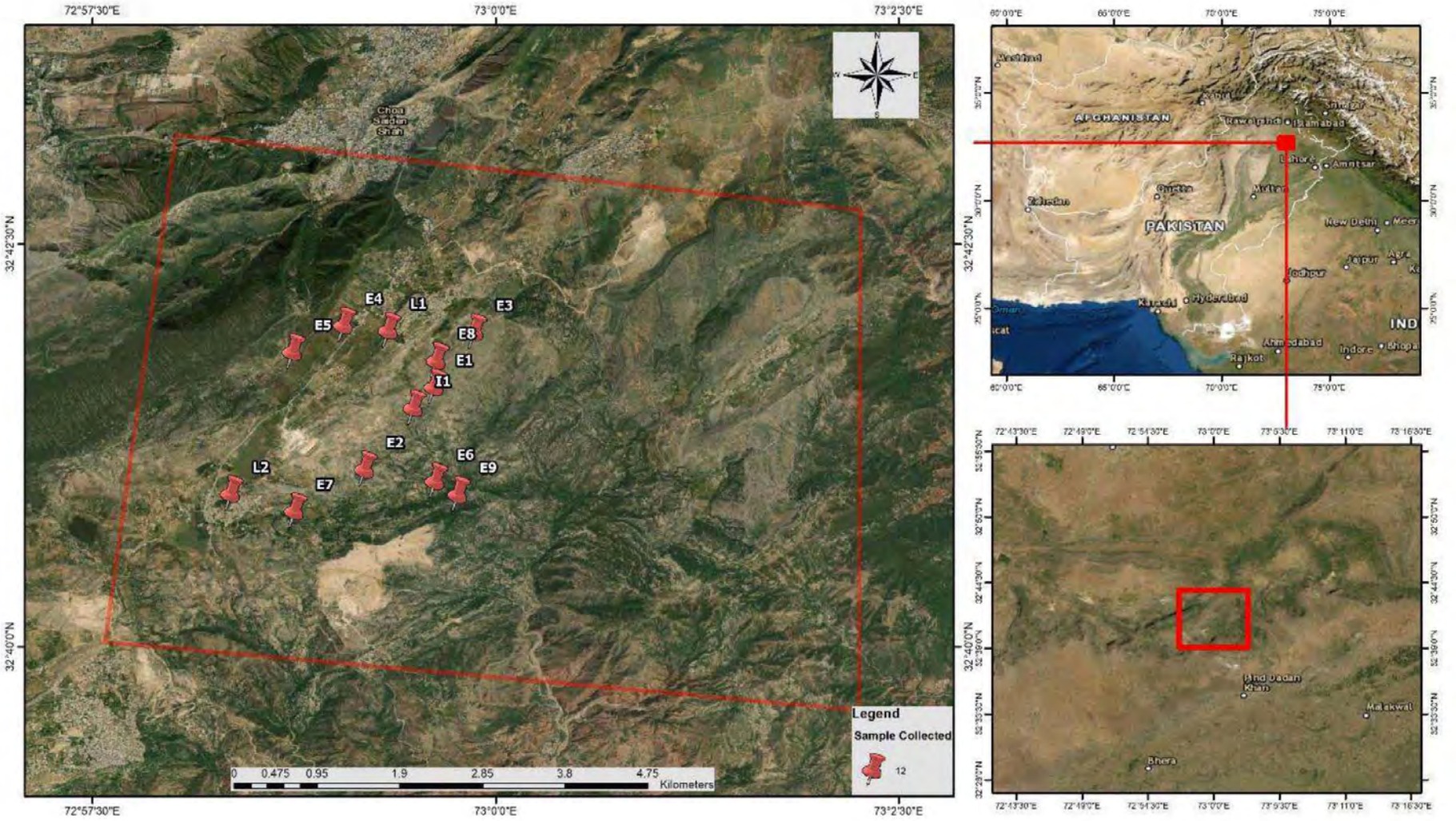

Figure 1.1 Satellite image of the study area, enclosed in a polygon, with sample collection points marked inside the polygon, prepared in ArcMap 10.4.

CHAPTER 02

GEOLOGY OF STUDY AREA

2.1 Introduction

The research area's geology, tectonic settings, and sequence stratigraphy all play important roles in hydrocarbon exploration. The geological history of the basin is used to piece together the basin's tectonic and depositional sequences (Kingston et al., 1983). Structural and geological information on the region is a key for translators to perform exact understanding of geophysical investigations. The fundamental explanation for that, by and large a comparable signature is gotten from various lithologies as well as the other way around. To manage such intricacies, an interpreter should have foundation information on geology about the region and its stratification, unconformities, and significant structures of region under study (Kazmi & Jan, 1997). This chapter deals with a brief description of tectonic settings, structural geology, and stratigraphy of the area under study.

2.2 Regional Geology of the Salt Range

2.2.1 Structural Settings

As depicted in Figure 2.1, the Salt range as well as the Potowar Plateau are referred as part of dynamic foreland network of fold and thrust belt of northern Pakistan’s Himalayas (Jaumé & Lillie, 1988; Gee & Gee, 1989; Pennock et al., 1989). Salt Range is a 175km long east-northeast oriented thrusting front which rises abruptly from the plain of river Jehlum. The Miocene and Pliocene epochs are traced as the ages of the Potowar thrusting (Raynolds & Johnson, 1985; Burbank & Raynolds, 1988). The Salt Range, with all its extension in the west, bends northwards and is delimited by a strike slip fault that runs north (McDougall & Khan, 1990; Baker, 1988; McDougall & Hussain, 1991; McDougall, 1988;). Thrusts migrate in the northeast trending anticlines in the Salt Range complex's eastern end (Pennock et al., 1989). The Salt Range joins with the Potowar Plateau in the north, typically a low relief highland excluding where it is pierced by the Soan river and its tributaries (Yeats et al., 1984).

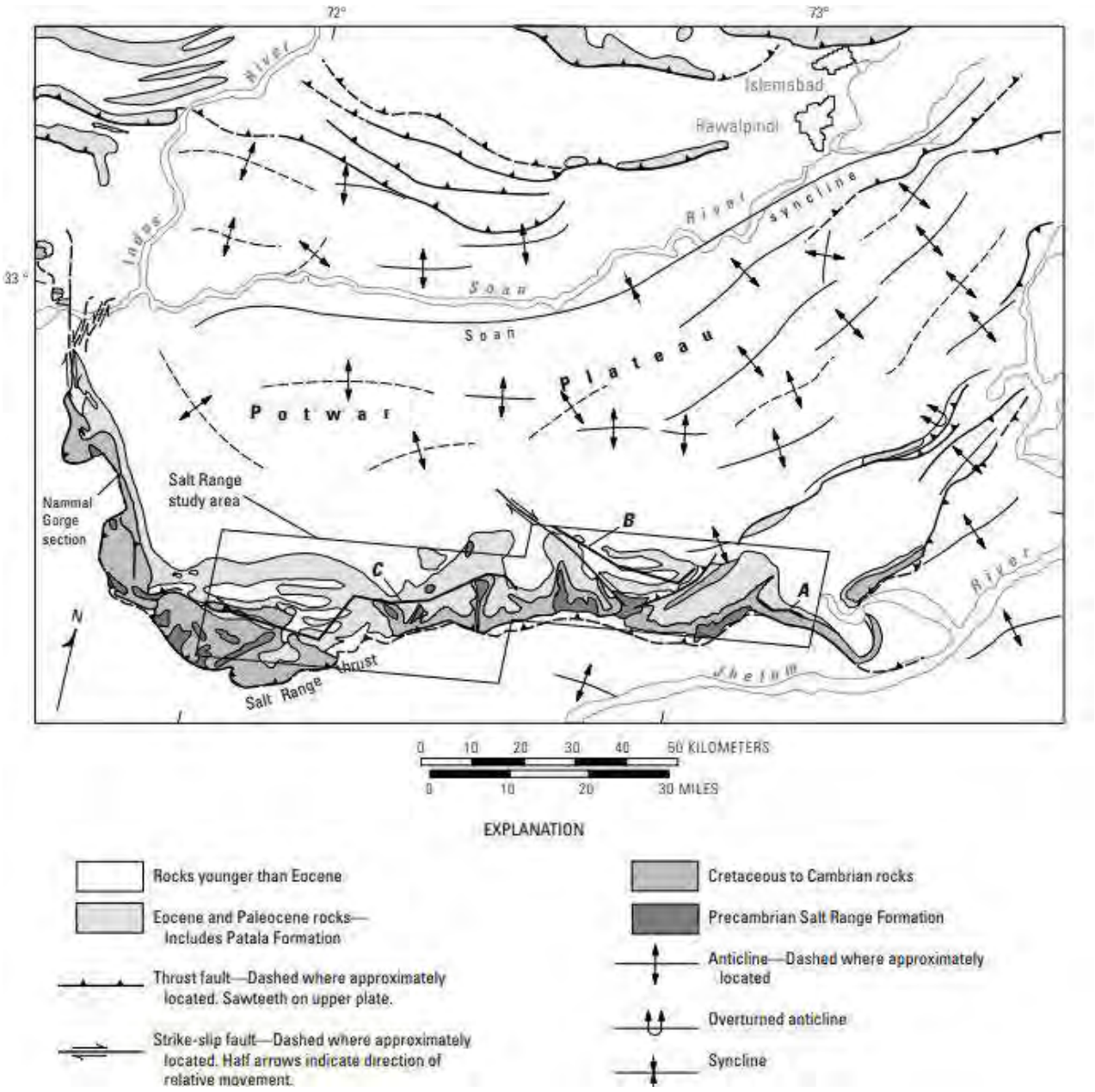

Figure 2.1Index map showing the location and generalized geology, with structural changes of the Salt Range study area (modified from Baker et al., 1988).

The Salt Range structures are limited zones of uplifted rocks, that are considerably highly faulted and folded in contrast to the low structural significance of the Potowar Plateau that usually comprises of broad folds, whilst the sedimentary rocks lack significant signs of deformative structures just south of the Salt Range (Yeats et al., 1984). The thrust's upthrown block brings the Salt Range Formation to the surface toward the southward facing margin of the overthrust wedge, that comprises of late Precambrian or Early Cambrian age evaporites as seen in Figure 4. These

evaporites underpin the Potowar Plateau and form a décollement zone enabling thrusting regionally (Jaumé & Lillie, 1988; Butler et al., 1987; Pennock et al., 1989).

A surprisingly well exposed record of sedimentary rocks of Cambrian, Permian, and newer layers sit on top of the Salt Range evaporites (Gee, 1980; Gee & Gee, 1989; Yeats et al., 1984). There are no rock bodies of the Carboniferous, Late Cretaceous, or Oligocene periods in the area, and there are substantial unconformities present in the study zone (Shah, 1980). This sedimentary series to the north of Salt Range dips steeply and is retained in the subsurface of Potowar Plateau's (Leathers, 1987; Baker et al., 1988). Drilling to the south of the Salt Range has revealed the absence of Cambrian to Eocene rocks (Baker et al., 1988).

2.2.2 Stratigraphy

Figure 2.2 shows how Paleocene coal and laterite containing rocks unconformably overlie Cambrian and Lower Permian strata in the Salt Range's eastern portion. Cambrian rocks (Baghanwala Formation) are composed of medium reddish brown to light red hue siltstone strata interbedded with mudstone and fine-medium granular sandstone (Khan and Khan, 1979; Ghauri, 1979). Lower Permian strata of Warcha sandstone and Tobra formation are mostly made up of interbedded clasts of conglomerates, mudstone, siltstone, and sandstones formed during the Gondwana glaciation (Middlemiss, 1892; Wynne, 1881; Ghauri, 1977; Reed et al., 1930; Reed, 1942; Schindewolf, 1964; Teichert, 1967; Medlicott, 1886; Law & Hussnain, 1989).

The Patala formation overlies the Hangu formation and Lockhart limestone in the Salt Range's eastern and central sections. With a thickness of (0-90m) Hangu formation is made up of nimble grey, burrowed, and somewhat calcareous strata of fine-medium granular sandstone that are typically ripple layered or flat plus interlayered of dark grey siltstone, mudstone, and lesser traces of carbonaceous shale. Eocene Lockhart limestone is composed of pale yellow nodular, skeletal wackstone to packstone and has a thickness of 5-70m. As illustrated in Figure 2.2, Lockhart limestone pinches toward the east in the eastern section of the Salt Range (Warwick & Shakoor, 1993).

Where Lockhart is lacking in the east, the bottom portion of Patala and the top portion of Hangu become indistinct, and the resulting unit has largely Patala traits, which was also noted with field observations displayed below in Figure 2.3. The Patala formation ranges in thickness from 5-90m

and is composed of interbedded claystone, mudstone, sandstone, siltstone, limestone, marl, coal, and carbonaceous shale.

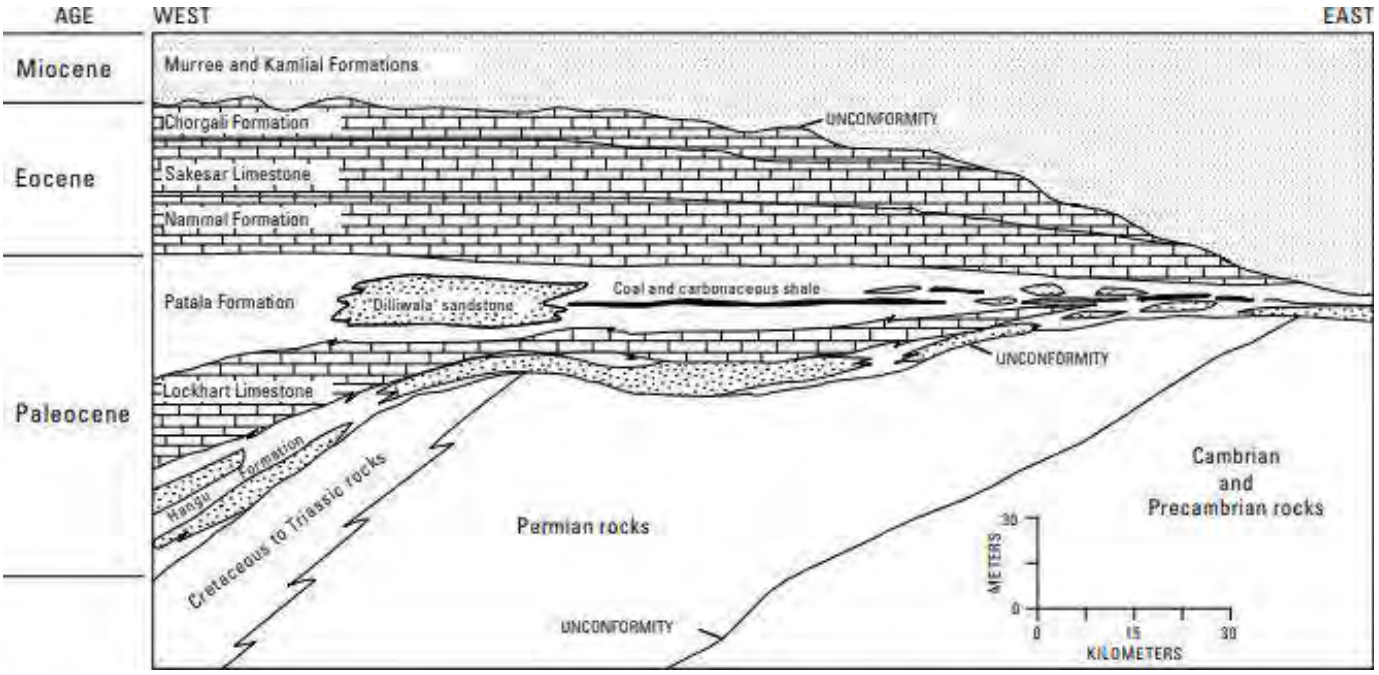

Figure 2.2 Generalized east-west longitudinal section of Tertiary formations in the Salt Range study area. Modified from Warwick and Shakoor, (1988). Stipple patterns, sandstone; brick pattern, limestone; no pattern, undifferentiated rock types.

The formation lies above the Lockhart, which is conformably overlain by thick (>100m) strata of Eocene age limestone composed of (1) Nammal Formation (nodular, skeletal mudstone to wackestone, marly, shaly), (2) Sakesar Limestone (skeletal wackestone to packstone, cherty, nodular to massive bedded,), and (3) Chorgali Formation (shaly, marly, nodular, skeletal (skeletal mudstone to wackestone and interbedded marl) (Wardlaw et al., 2007; Shah, 1980; Jurgan and Abbas, 1991; Jurgan et al., 1988;). These limestones are then overlain by Miocene age strata of Murree and Kamlial formations that lie unconformably, comprising of layers of green-gray and brown, massive coarse granular to pebbly sandstone contrasting with brown and red clay (Gee, 1980), as illustrated in Figure 2.2.

Figure 2.3 Hangu formation and Patala formation sharing similar characteristics as observed in the study area with mudstone, siltstone and sandstone bodies intermixed with shales of Patala formation, with the pen used as a scale of observation.

2.3 Eastern Salt Range

Figure 2.4 of the east-west longitudinal section depicts the lithofacies distribution in the Salt Range's eastern zone, where outcrop findings show that conglomerates of Tobra formation and Lower Permian Warchha sandstone fill stream scours indented into the Cambrian Baaghanwala formation that underlies the Warchha sandstone having a 30m erosional relief (Warwick & Shakoor, 1993). In the eastern Salt Range Patala formation is characterized by quartzose and type 3 sandstone lithofacies occurring at its base, which are usually associated with Permian sandstone and conglomerate contact.

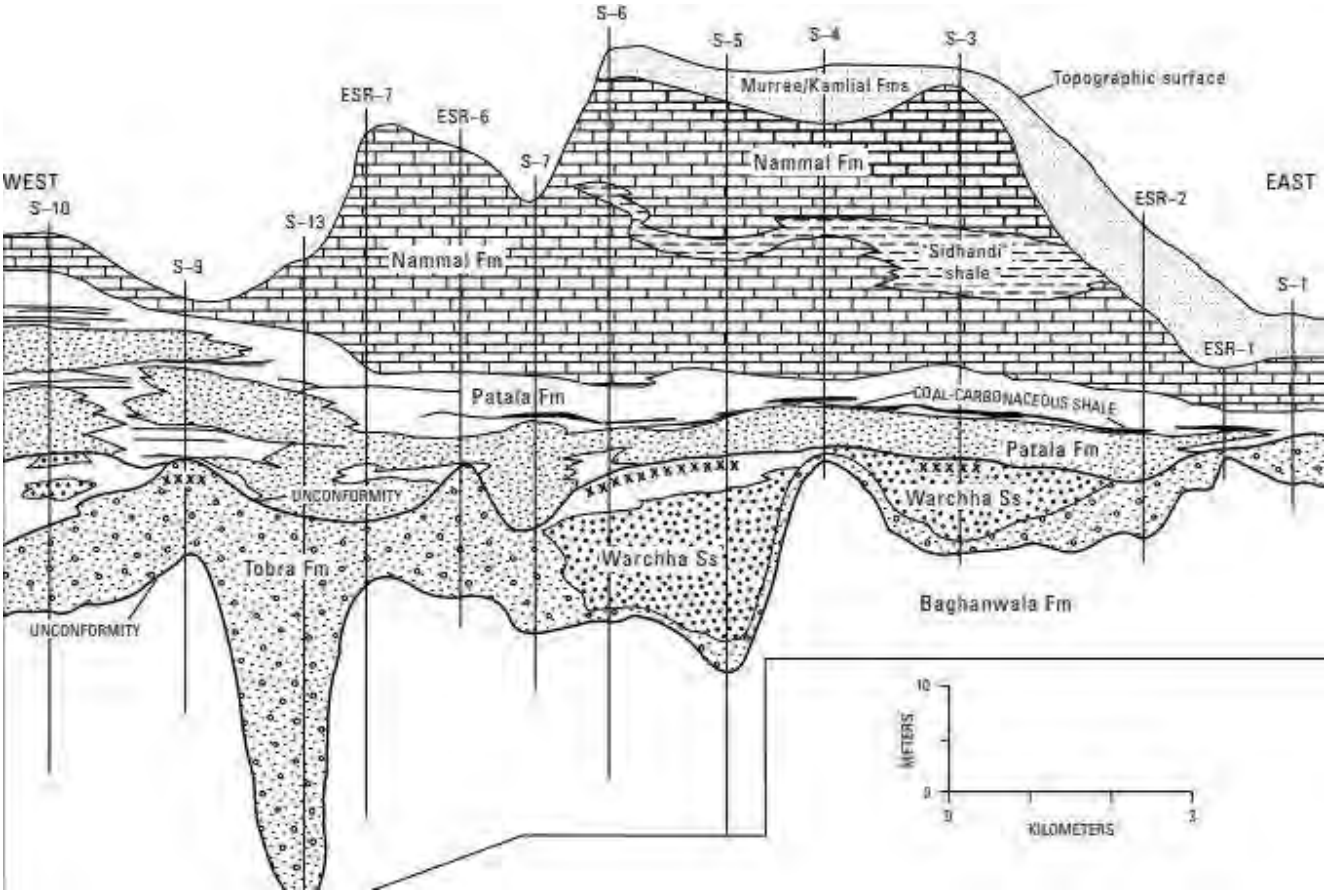

Figure 2.4 Detailed east-west longitudinal section of the coal-bearing and associated rocks in the eastern part of the Salt Range coal field. The section numbers used in this study refer to those used in Warwick and Shakoor, (1988), who gave detailed locations, references, and lithologic descriptions for each section or drill hole. Datum for the cross section is the coal-bearing zone. Key marker beds in each section or drill hole were used for correlation. Fm(s), Formation(s); Ss, Sandstone; three stipple patterns, sandstone in the Murree and Kamlial Formations, Patala Formation, and Warchha Sandstone; brick pattern, limestone; no pattern, mixed siltstone, mudstone, and marl; stipple pattern with circles, conglomerate and diamictite; XXXX, weathered paleosurface.

Laterite & bauxite deposits are typically found close to the bottom of Paleocene sections in the eastern portion of Salt Range. Below the Paleocene unconformity in parts weathered parent rock is even maintained; however, the bauxite and laterite layers were later replaced by type 3 sandstone dominated bodies (Warwick & Shakoor, 1993).

The eastern Salt Range's major sandstone deposits, type 2 and type 3 sandstone deposits, occur piled, with a thickness of 15m. Type 3 sandstones have steep base overlying the Tobra Formation, Baghanwala Formation, or Patala Formation. Cumulatively thick sandstone formations in various regions are characterized by type 3 sandstone formations that stretch mostly in northerly direction with increasing sandstone thickness toward their axis. The most extensive of these regions where

sandstone thickness surpasses 9m occurs in between longitudes of 73° 05'E and 73° 10'E, with a nominal thickness spanning 6 to 12m and a width of more than 3 km.

Sandstone bodies accumulated in the eastern Salt Range reflect barrier system deposits. Certain observations are crucial in supporting this interpretation. (1) plentiful trough, tabular, bimodal, and stratification with low angle of sandstones characterized as type 3; (2) elongated and discontinuously shaped accumulated sandstone deposits; (3) affiliation with brackish maritime rocks; (4) occurrence of quartzose sandstone; and (5) similarities of sedimentary structures and sandstone body types found in Salt Range and other barrier island deposits (Staub & Ferm, 1979; Moslow, 1984; Galloway & Hobdy, 1983). Internal sedimentary features inside bodies characterized by type 3 sandstone with comparative elongation adjacent to Patala formation, where numerous tidal channels whose deposits, together with beach foreshore sandstones, predominate preserved succession, suggest the bodies were produced along a shoreline (Warwick & Shakoor, 1993).

2.4 Lithofacies of Interest

2.4.1 Sandstone

- Type 1 sandstone is composed of fine-grained, flat to ripple-bedded sandstone beds and are only thick in few centimeters occurring mostly with intervals that are influenced due to siltstone and claystone lithofacies, with some of the sandstone bodies interlayed with impure coal or carbon - containing shale of Patala formation and so can be rooted out, with the lateral sequence reaching up to 20m (Warwick & Shakoor, 1993).
- Type 2 sandstone is observable horizontally up to 100m and consists of 2m thick uninterrupted tabular bodies with fine-medium grained, undulating bedding, cross stratified or ripple lamination, lithofacies and (0.25m thick) small trough and tabular cross bed sets (Warwick & Shakoor, 1993). The upper interface is normally gradational, while the bottom contact is generally abrupt with underlying sediments. Frequent occurrence of burrows which are generally filled with pyrite which can be observed below in Figure 2.5. Most burrows resemble those produced by thalassinidean shrimp (Bromley & Frey 1974). Type 1 sandstone grades into type 2 sandstone and these sandstone lithofacies usually occur together in mudstone dominated intervals.

- Type 3 sandstone lithofacies can be traced horizontally for several kilometers and have a thickness of much more over 5m. The grain size of such sandstones varies from moderate to pebbles, and they are all quartzose. These sandstones often have a fining upward grain structure, with top contact with the overlaying strata being gradational. Ripple lamination, planar beds, tabular cross stratification and trough to broad low angle, characterize the sedimentary structures (Warwick & Shakoor, 1993). Trough and tabular cross stratified beds up to 0.5m thick and 2m broad with inner scour characteristics exist with interior scour characteristics and thus are persistent horizontally as of the outcrop. In the upper half of the sandstone's claystone interbeds which contain drapes of claystone overlie at reactive surfaces characterized by ripple lamination.

Figure 2.5 Type 2 sandstone bodies with burrows by thalassinidean shrimp filled with pyrite as observed through literature analysis, with the pen serving as scale of observation.

2.4.2 Laterite Beds

The Salt Range's Paleocene rocks (made of Hangu and Patala formations due to their identical characteristics) are formed of whitish giant claystones and hematite loaded mudstone-like rocks in the lower 5m. The claystones with a thickness of up to 10m are interbedded with mudstones that are hematite rich and can be seen below in Figure 2.6 (Ashraf et al., 1972; Hassan, 1985; Abbas & Hassan 1985; Whitney et al., 1990). These mudstones are less than 3m thick and have a pale to reddish brown tint with root imprints and beige to reddish brown glaebules (circular masses) up to 3cm in diameter. In coal field locations, such clay or mudstones were overlain by coal layers or carbonaceous shale and type 3 sandstones and underlain by weathered Cambrian or Permian rocks. More than one hematite rich mudstone bed may occur in the lower 5m of the Paleocene rocks in the area, with Whitney et al., (1990) assessment of the claystone specimens and imply the principal composition of minerals including gibbsite, boehmite, and kaolinite, while the mudstone samples generally comprise of lepidocrocite, goethite, hematite, and a wide range of Fe oxides and oxyhydroxides.

Figure 2.6 Hematite rich mudstone bed may occur in the lower 5m of the Paleocene rocks in the area with beige to reddish brown glaebules (circular masses) and pen used as scale of observation.

Massive claystones are understood as bauxites, while hematite-rich mudstones are viewed as laterite Whitney et al., (1990). According to Warwick and Shakoor (1993), the bauxite and laterite deposits indicate a horizon of paleosols that formed on the surfaces of exposed Cambrian and Permian strata or pre-transgressive Paleocene rocks. Organic matter, which is also the abundant carbonaceous shales and coal beds, overlies the bauxites and laterites in places where the transgressive upper shoreface processes did not remove it. Bauxites are readily formed in areas with heavy non - seasonal rainfall, tropical forests, silica poor, base rich source materials, and near neutral pH (Young & Goudie, 1973; Retallack, 1989). However, the process of development of laterite is still debated; it may form in areas with large concentrations of rainfall, distinct dry seasons, and mild temperatures resembling the subtropical to tropical range (McFarlane, 1976; Retallack, 1989). The occurrence of bauxite and laterite in connection with Salt Range's Paleocene unconformity indicates tropical to subtropical climates. Because to the Indian subcontinent's equatorial position during the Late Cretaceous and Paleocene periods, such climate is expected (Molnar & Tapponnier, 1975). Laterite has been used to describe red and yellowish-colored ferruginous exposures, and lateritic bauxite has been used to describe whitish, orange, and mild, bluish-coloured ferruginous and aluminous rocks.

2.5 Sampling and Chemical Analysis

A total of 12 exposure samples were taken in account before yielding to any other investigative technique to be employed in the study area. Fresh samples taken showed oxidization on the surface and rusting within the rocks, thus indicative of the presence of ferruginous content in high quantity. Moreover, the samples were carefully analysed in the laboratory where the technique of X-Ray Diffraction (XRD) with a copper anode, having a divergence slit of 1.52mm in a range of 5 to 80 which was continuously scanned, was utilized for determining the mineral quantity, where the chemical analysis result showed that the samples contained high percentage of silica, alumina, and iron oxide, is given below in Table 1.

Table 1 Geochemical Analysis of percentage amount of content present at given latitude and longitude of sample collection.

Sr. No	**Latitude**	**Longitude**	**SiO_2**	**Fe_2O_3**	**Al_2O_3**
E1	32° 41' 37.01" N	72° 59' 37.69" E	44%	30.2%	25.8%
E2	32° 41' 6.31" N	72° 59' 11.88" E	23.5%	44.1%	32.4%
E3	32° 41' 57.41" N	72° 59' 52.63" E	45.8%	30.3%	23.9%
E4	32° 42' 0.00" N	72° 59' 4.00" E	62%	25%	13%
E5	32° 41' 50.00" N	72° 58' 45.00" E	80.8%	12%	7.2%
E6	32° 41' 1.88" N	72° 59' 38.00" E	66.7%	18.7%	14.6%
E7	32° 40' 50.72" N	72° 58' 45.71" E	67.8%	20.4%	11.8%
E8	32° 41' 46.76" N	72° 59' 38.61" E	45.3%	37.9%	16.8%
E9	32° 40' 56.94" N	72° 59' 46.45" E	65%	23%	12%
I1	32° 41' 29.17" N	72° 59' 30.02" E	64.4%	24.7%	10.9%
L1	32° 41' 57.95" N	72° 59' 20.66" E	45%	40%	15%
L2	32° 40' 57.20" N	72° 58' 22.02" E	66%	18%	16%

2.6 Reserves

Total length (L) of the exposures is estimated to be about 1611.2m, and by taking average thickness (T) of the laterite beds as 3m with specific gravity (g) taken as 2.8, and the dip distance as 30.0 reserves of ferromagnetic laterite bodies can be calculated as 0.41 million tonnes using Equation (1):

$$Tonnage = L \times T \times Dip\ Distance \times g. \quad (1)$$

CHAPTER 03

APPLICATIONS OF REMOTE SENSING

3.1 Introduction

With mankind reaching far outskirts of the solar system, using satellite technology has been a marvel of technology, but similarly this advent has been keenly utilized to study the key geological and mineral features present on earth. Geological maps representing the outcrops of surface pattern, that may show bed rocks, define boundaries of strata of outcrops represented in geological maps. Orthodox mapping techniques or mineral investigations is based on labor intensive and experimental methods to extrapolate and interpolate map making that is hard, time consuming, and costly at the same. Satellite data helps overcome this wellspring of data, moreover, the geological highlights of earth can be distinguished in the bedrock outcrops through air surveillance, or from remote sensing imageries. Sensors onboard the satellites have precise abilities that enable them to quantify physical aspects of surface such as spatial, spectral, and radiometric resolutions, viewing angle, acquisition time, etc. This digital information of the image is georeferenced and present as data for geological mapping, with several researchers proposing the use of hyperspectral and multispectral remote sensing data sets as best utilized for surface feature mapping and lithological discrimination (Ryerson & Rencz, 1998).

3.2 ASTER Sensor

The Advanced Spaceborne Thermal Emission and Reflection Radiometer (ASTER) was deployed on NASA's Terra (formerly designated EOS AM-1) spacecraft in December 1999. (Yamaguchi & Naito, 2003). ASTER is comprised of three vital sensors that have three spectral bands of visible and near infrared VNIR, six bands of SWIR, and five bands of TIR with spatial resolutions of 15m, 30m, and 90m, respectively, and further spectral ranges of each band are described below in Table 2. ASTER data has high quality spatial resolution and unique arrangement of wide spectral coverage and is of peculiar importance to remote sensing in relation to studies for geology since it provides a comparatively vast spectral range and fine spatial resolution, due to such an advantage ASTER images have been utilized time and again for geological purposes (Gad & Kusky, 2007).

Table 2 ASTER spectral band width along with each band specified central wavelength and spatial characteristics of each band.

ASTER			
Bands	Spectral Range (μm)	Central Wavelength(μm)	Spatial Resolution
1	0.520-0.600	0.560	15m
2	0.630-0.690	0.660	15m
3	0.780-0.860	0.810	15m
4	1.600-1.700	1.650	30m
5	2.145-2.185	2.1650	30m
6	2.1825-2.225	2.205	30m
7	2.295-2.285	2.260	30m
8	2.295-2.365	2.330	30m
9	2.365-2.430	2.395	30m
10	8.125-8.475	8.300	90m
11	8.475-8.825	8.650	90m
12	8.925-9.275	9.100	90m
13	10.250-10.950	10.600	90m
14	10.950-11.650	11.300	90m

ASTER has made use of the observation of reflecting solar irradiance by developing six spectral features of the SWIR observatory that aid in the differentiation of various elements such as AlOH, Fe, MgOH, and SiOH (Kahle et al., 1995).

3.3 Optimization of ASTER Data

When comparing the ASTER sensor with Landsat, for geological and non-geological investigations Enhanced Thematic Mapper (ETM+) images of Landsat are regarded as popular base maps (Bamousa, 2011). In Figure 6 comparison between ASTER sensor bands such as VNIR, SWIR and TIR and Landsat (ETM+) telescope bands is observed (Adams & Gillespie, 2006). Landsat (ETM+) bands 2, 3 and 4 are equivalent to the bands 1, 2 and 3 of VNIR telescope, that detect the visible electromagnetic radiation (EMR) as seen in Figure 6. Bands 5 and 7 of ETM+ are equivalent to the bands 5-9 of SWIR sensor, whereas band 6 of the ETM+ is similar to bands 10-14 of the TIR sensor shown below in Figure 3.1. Bands 1-9 of the ASTER sensor are reflected

as well as 1-5 and 7 of the Landsat ETM+, whereas ASTER bands 10-14 and Landsat ETM+ band 6 are emitted. Landsat ETM+ sensor bands 1-4 are visible, bands 5 and 7 are infrared and band 6 is thermal infrared. For studies of non-geological bodies visible bands are suitable, while geological bodies can be best studied with the help of infrared bands (Vainer et al., 2020).

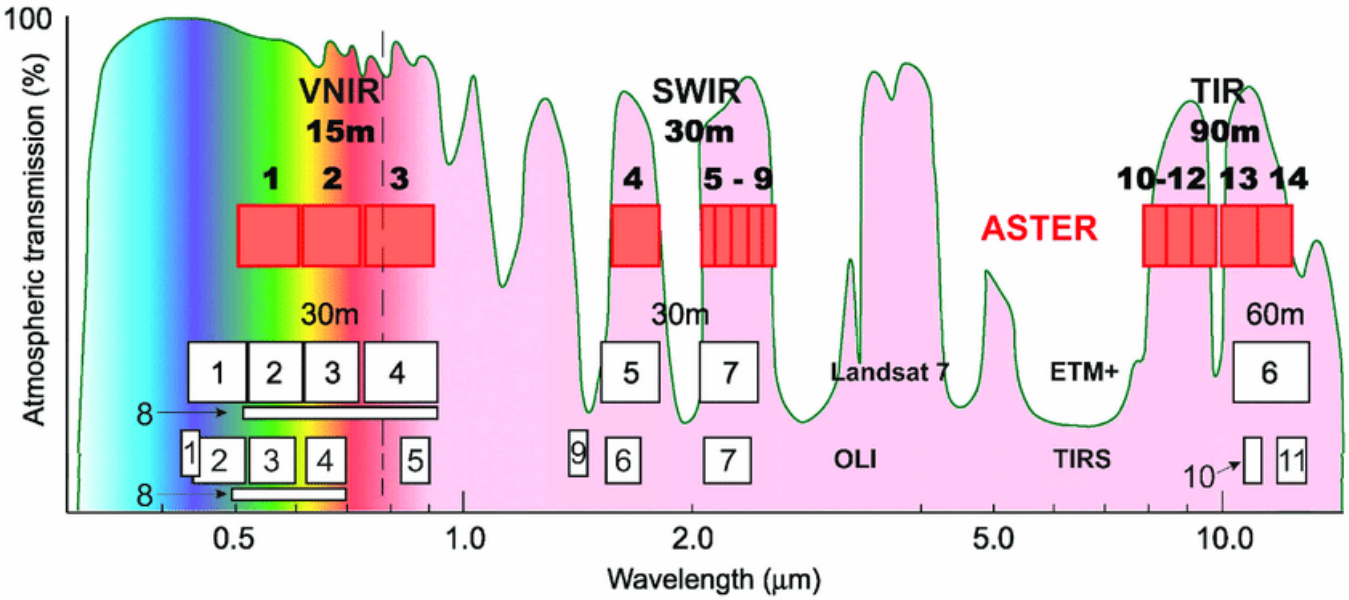

Figure 3.1 Electromagnetic spectrum comparing ASTER and Landsat (ETM+ and OLI/TIRS) bands. The spatial resolution for bands in the VNIR, SWIR and TIR are specified for each sensor. The vertical dashed line represents the end of the visible light (Testa et al., 2018).

3.4 Processing

3.4.1 Data Acquisition and Computer Software

ASTER data is favoured considering the accessibility of cloud free imagery, the nature of the picture, and the hour of obtaining (NASA Land Processes Distributed Archive Centre). The picture was at first seen and picked by means of https://lpdaac.usgs.gov/and pre-processed utilizing ENVI programming schedules, which performed climatic revision and changed radiance information over to reflectance products (VNIR and SWIR) pictures.

ASTER data was then preprocessed using ENVI 5.3 (spectral image processing software), where the processed imagery was then compiled with other datasets using ArcGIS 10.4 geographic information system (GIS) software.

3.4.2 Preprocessing of ASTER Data

Although the ASTER data has been properly calibrated, preprocessing is still an important step in acquiring information on the tiny differences of rock units. Surface items such as cloud, frost, seas,

rivers, and margins must always be masked since their spectral characteristics differ significantly from those of alteration minerals. Masking gives a visual representation of tiny variations in alteration mineral deposits in alteration zones while using BR or PCA. Densely vegetated areas must also be masked to achieve reliable outcomes from alteration zones, because when only SWIR bands are used, the vegetation is treated as an alteration throughout analysis and processing.

The study is performed on an ASTER level 1B image, that is already accounted with terrain correction and crosstalk correction. The VNIR ASTER data having spatial resolution 15 was resampled to 30m to correspond with SWIR data using nearest neighbor resampling method, thus, VINR and SWIR bands were stacked forming 9 bands with the spatial resolution of 30m.

The Fast Line of Sight Atmospheric Analysis of Spectral Hypercubes (FLAASH) algorithm (Perkins et al., 2012; Cooley et al., 2002) the VNIR-SWIR ASTER radiance database components were modified to eliminate the effect of the atmosphere, allowing the data to be translated into a luminescence database to surface reflectance. Lithological features were then digitized from geological map at a scale of almost 10km of the area. The map was later used as an input dataset for remote sensing image interpretation to identify the mineral bodies of interest in the study area. All the data pre-processing procedures were implemented by ENVI software, and the visualisation and mapping were conducted on the ArcGIS platform.

3.5 General Methodology

Several techniques have been encompassed in the study to identify lithological features, source of deposition, structural feature and minerals of interest of the study area, the flow chart of the general methodology can be seen below in Figure 3.2, which is based on several steps, from literature review to understand general geology, to field data collection to review the mineral of interest present in the study area, followed by pre-processing and data interpretation of the ASTER dataset.

To clearly visualise the image, the pre-processing steps spanned from FLAASH Atmospheric Correction, Post FLAASH Atmospheric Correction and image enhancement were embarked upon, whilst implementing the processing techniques, the image of study was georeferenced onto the projection system of WGS84.

After this the techniques employed for visualisation of the data set which were PCA, band rationing and advanced mineral mapping, helping in the discrimination of the lithological units of the area

and with cross validation of the above techniques with the field sample data, and geophysical investigation of study area were utilized.

The information provided by the spectral properties of the terrain is vital for discriminating rock kinds, and multispectral colour composite images are the most dependable. When looking at the possibility of number of three colour options which can be deduced from all the bands, the collection of three bands from provided reflected channels of ASTER image is time consuming. For this, quantitative optimization formulae of the bands for colour composites occur, based on statistical approaches (Sheffield, 1985).

Although the results are not always aesthetically pleasing for qualitative interpretation, the Crósta method is considered as an effective approach for collecting information on alteration zones by applying PCA to Landsat data (Crósta et al., 2003; Loughlin, 1991). The Crósta method was used to analyse the ASTER data.

Combinations of ASTER bands utilized by earlier authors to discern between rock types in comparable climatic settings (http://www.ga.gov.au/imagecache/GA7833.pdf) (Kalinowski & Oliver, 2004) were shown to be useful in this location. The notion that human vision is more susceptible to variations in saturation and intensity in blue colours but less so in red and green hues influenced display colour allocation (Crósta et al., 2003).

3.6 Results After Correction

At first cross talk correction was applied to remove the leaching effect of band 4 of the SWIR band into bands 5 and 6, that would disrupt the data, after which a process of stacking layers was applied on the VNIR and SWIR bands, which made the data set ready for the application of FLAASH Atmospheric correction as shown below in Figure 3.3.

The FLAASH Atmospheric correction carefully applied, was then made ready for post FLAASH Atmospheric Correction using a formula referred to as band math functioning on the basis of pixel value being greater or equal to 10,000, so it is multiplied to one, but if the pixel value is greater than zero and less than 10,000 then it is multiplied to its float value and the result to be divided by 10,000, that applies to each of the nine bands stacked together, with its result shown below in Figure 3.4.

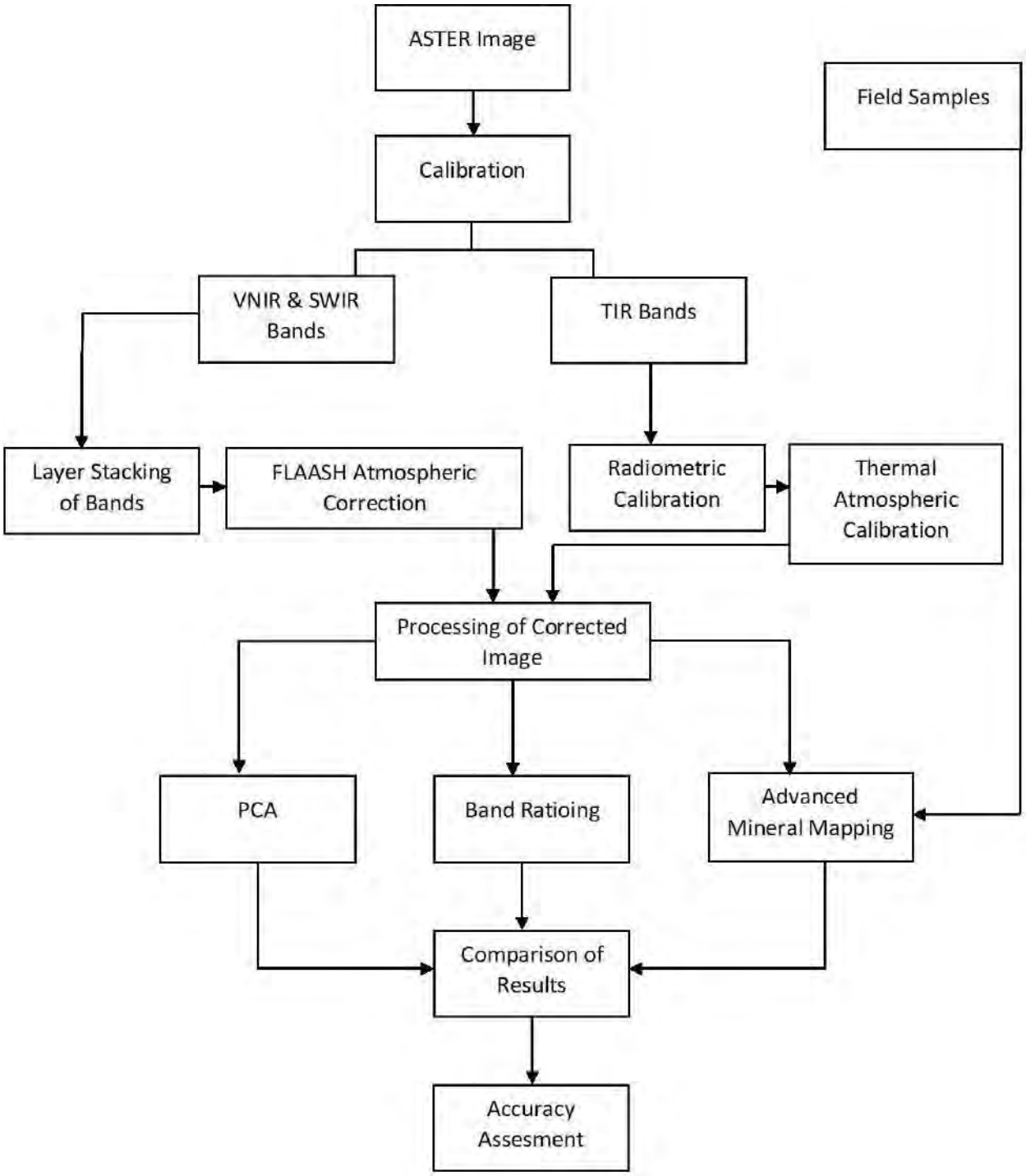

Figure 3.2 ASTER workflow methodology followed in processing and obtaining results and comparing with the geological and geophysical data.

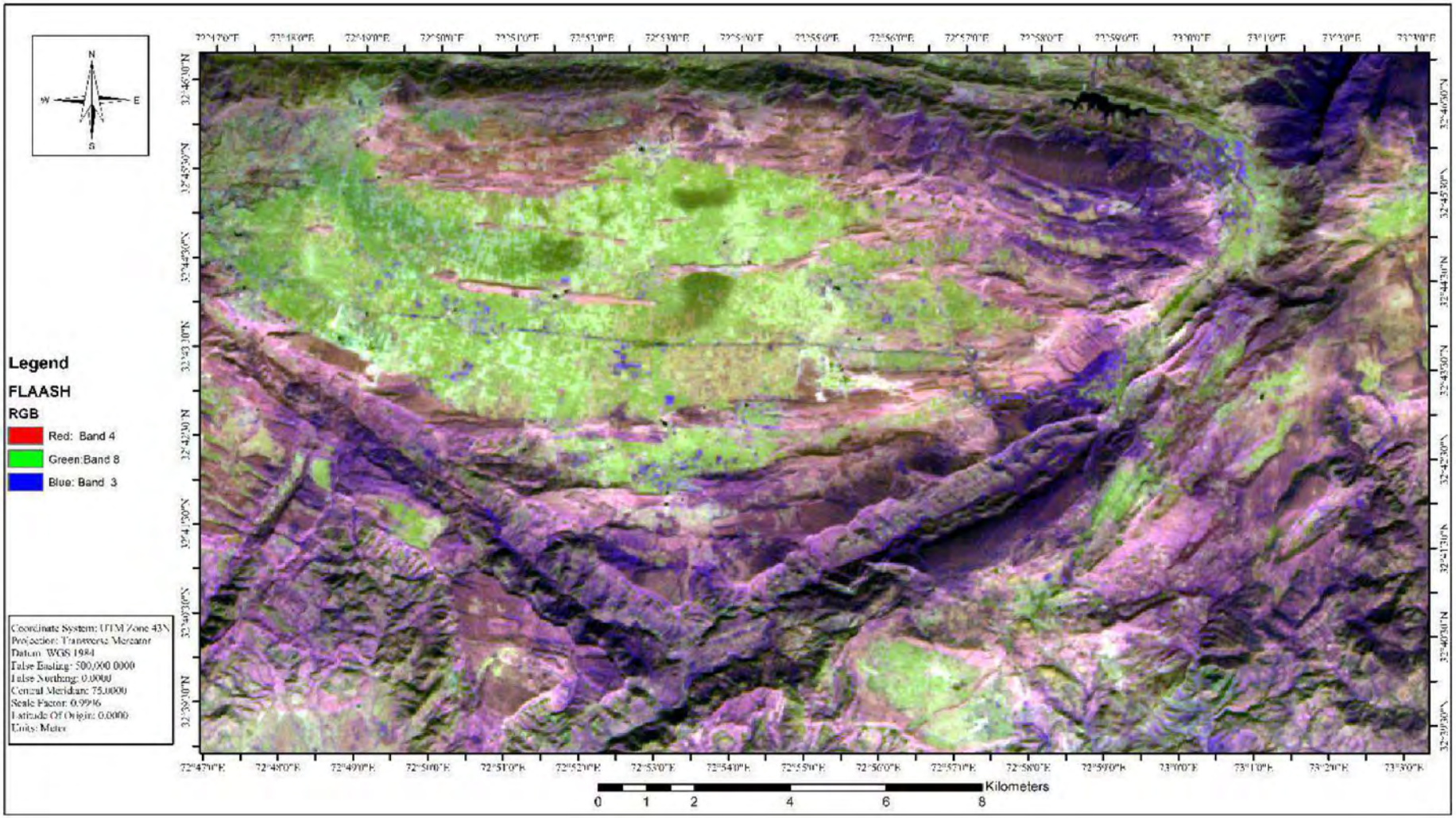

Figure 3.3 ASTER satellite imagery obtained after application of FLAASH atmospheric correction, with RGB of bands 4,8 and 3 utilized in ENVI 5.3 software and image compiled in ArcMap 10.4.

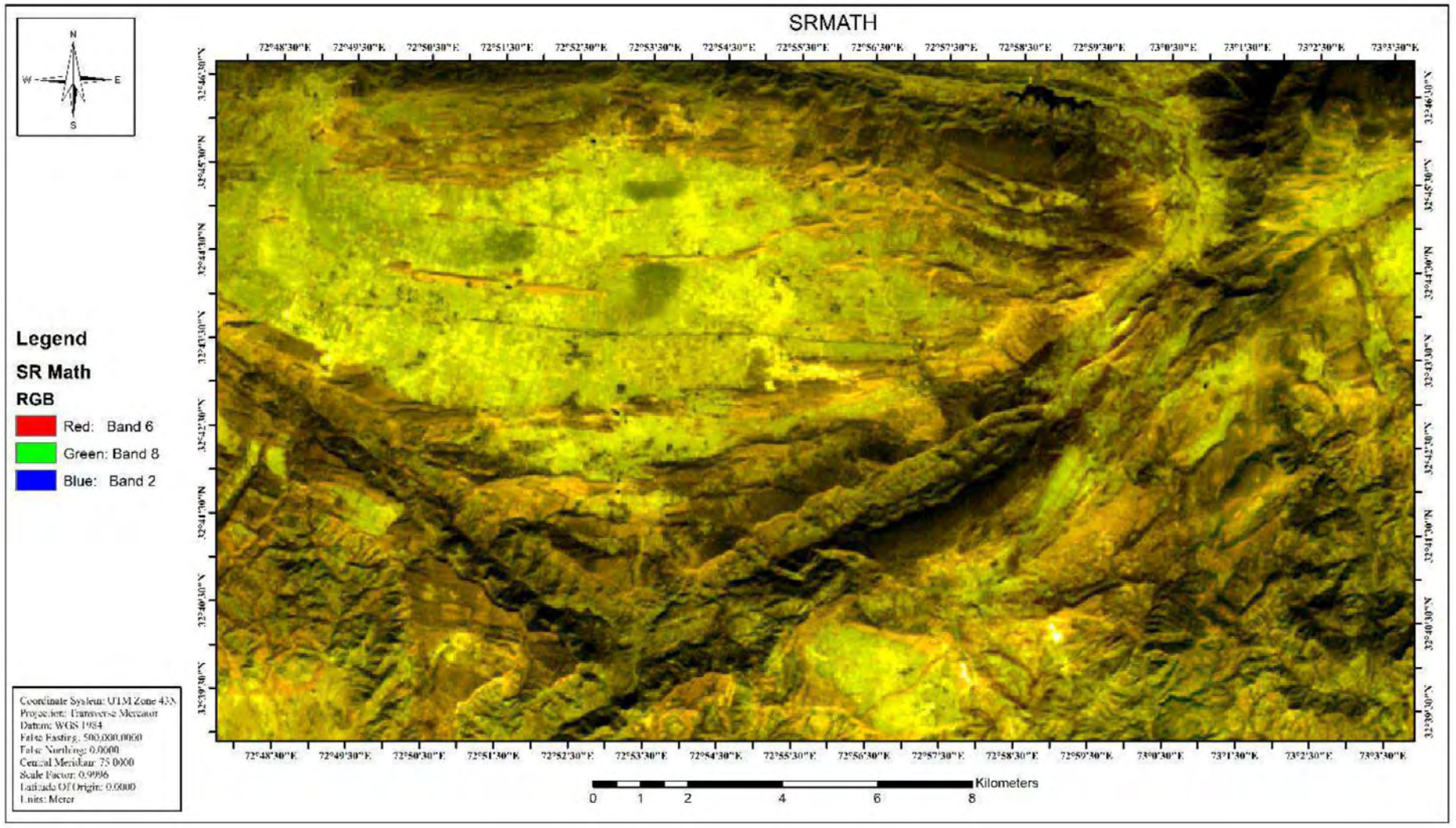

Figure 3.4 ASTER satellite imagery obtained after application of FLAASH atmospheric correction on which spectral math (band math) was applied to further enhance the wavelength, with RGB of bands 6, 8 and 2 utilized in ENVI 5.3 software and image compiled in ArcMap 10.4.

3.7 Techniques

3.7.1 Principal Component Analysis (PCA)

The correlation coefficient of 9 ASTER band of VNIR and SWIR bands stacked together is often greater than 0.9, so PCA has been performed on these 9 ASTER bands to decorrelate the data and lower the dimension of the study area (Richards, 1999). PCA is a multimodal statistical method based on the linear algebraic matrix operations that is commonly used for multispectral picture interpretation. PCA works on the principle of selecting uncorrelated linear combinations (eigenvector loading) of factors in a way causing each of the components to extract the linear combination with reduced variance. The main aim is generation of a set of new orthogonal axes with origins at the mean of the data which are then rotated in an order that minimizes variance (Pour & Hashim, 2011). The number of outputs PCA bands equals the number of input spectral bands. When particularly in comparison to the other bands, where it can be seen the first band of PCA has the highest percentage of variance data, while the second band of PCA does have the second highest percentage of variance information, etc, however the last band of PCA does seem to be noisy because it contains information with very little variance which is attributable to the noise in original spectral data (Pour & Hashim, 2011).

3.7.2 Band Ratio (BR)

Detection of traits that are comparable to technique of BR can be used to improve spectral performance. This is an image enhancement approach that involves dividing the digital number (DN) readings in one spectral range by the corresponding parameters in another band. One of the key advantages of the BR technique is these BR images represent the spectral or color properties of image features regardless of differences in scene illumination conditions (Carper et al., 1987). Band ratios helps in highlighting certain features that cannot be visualised in raw bands (Rowan et al., 1977).

3.7.3 Advanced Mineral Mapping

Following the application of band ratios, a statistical technique was used using background threshold values, and the predicted abnormalities of each band ratio image could be determined using one of the following equations (2-4).

$$TH = M + 3 * SD, \quad (2)$$

$$TH = M + 2 * SD, \quad (3)$$

$$TH = M + SD. \quad (4)$$

Here the confidence percentage of Equation (2) being 98%, Equation (3) being 95% and Equation (4) being 92%, and M is the mean pixel value, while TH being threshold pixel value, and SD as standard deviation.

Application of remote sensing for tracing out minerals of interest is a widely major task of this study, but it also has two major comparisons. Firstly, between the different band combinations in different classification techniques i.e., which specific band combination applied in the techniques provides with the most reliable result and secondly the comparison between different techniques itself that which technique provides the most visually interactive and best possible result.

3.8 VNIR and SWIR Bands

3.8.1 PCA

Various PCA combinations were utilized in conjunction to delineate lithological setup in the area of interest, with primary focus on the ferrous oxide lateritic beds, with the combinations used and their interpretations made using ground truth points are as follows:

3.8.1.1 PCA Combination 9, 2, 1

The first calculation of PCA 9, 2, 1 was calculated and layer stacked with the same patten and classified as RGB, where in the laterite bed was specifically targeted which can be visually represented with dark green hue, whereas the clay deposits in the area came out with a sky-blue colour and the carbonates and sands in the formation represented by dark blue colour, as shown below in Figure 3.5.

3.8.1.2 PCA Combination 7, 5, 4

The second combination of PCA 7, 5, 4 with similar RGB combination were calculated and stacked where the lithological setup was minimally described but key structural features were noted in the image. A major left lateral strike slip fault with a more yellowish hue was noted which moved along the main Choah Saidan Shah road separating the north east trending Dil-Jabba thrust from the Salt Range thrust, similarly another small strike slip feature parallel to the major strike slip fault ran along in the study area with a turquoise hue which is one of the reasons for the terrain being more rugged, and the structural feature most prominent, which in geology can be pinned as a reason of the unconformity along with the stratigraphic unconformity of the study area as seen below in Figure 3.6.

3.8.1.3 PCA Combination 3, 1, 2

The third combination of PCA 3, 1, 2 was calculated and layer stacked with the same pattern classified as RGB respectively. In this image several different hues of colour outlining the lithological setup were noted, with hues of sky blue to turquoise representing the clay or unconsolidated deposits in the study area, the green hues representing the Eocene carbonates exposed on the surface, the parrot green to yellow colour representing the sand bodies of Permian age , while the pink colour integrating in the purple hue representative of the Palecone age rocks with the purple colour also being the dominant representation of the laterite beds of interest in the study area, shown below in Figure 3.7.

3.8.1.4 PCA Combination 1, 2, 3

The final combination of PCA 1, 2, 3 was calculated and layer stacked and classified RGB with the same pattern, delineating lithological setup remarkably with different hues of colour. The most dominant colours being yellow, light green, pink, blue and parrot green in some areas. At first the yellow colours are most dominantly in areas of clay minerals, with the pink colours dominant of Eocene carbonates exposed in the area. The light green colour hits at the area in focus mostly which correlates with the field data of laterite exposures in the area, while the parrot green colour correlates to the sandstone bodies of Paleocene rocks or in the southeast where the sand bodies are of Paleocene and Permian rocks, due to the arising unconformity in the study area, which can be seen below in Figure 3.8.

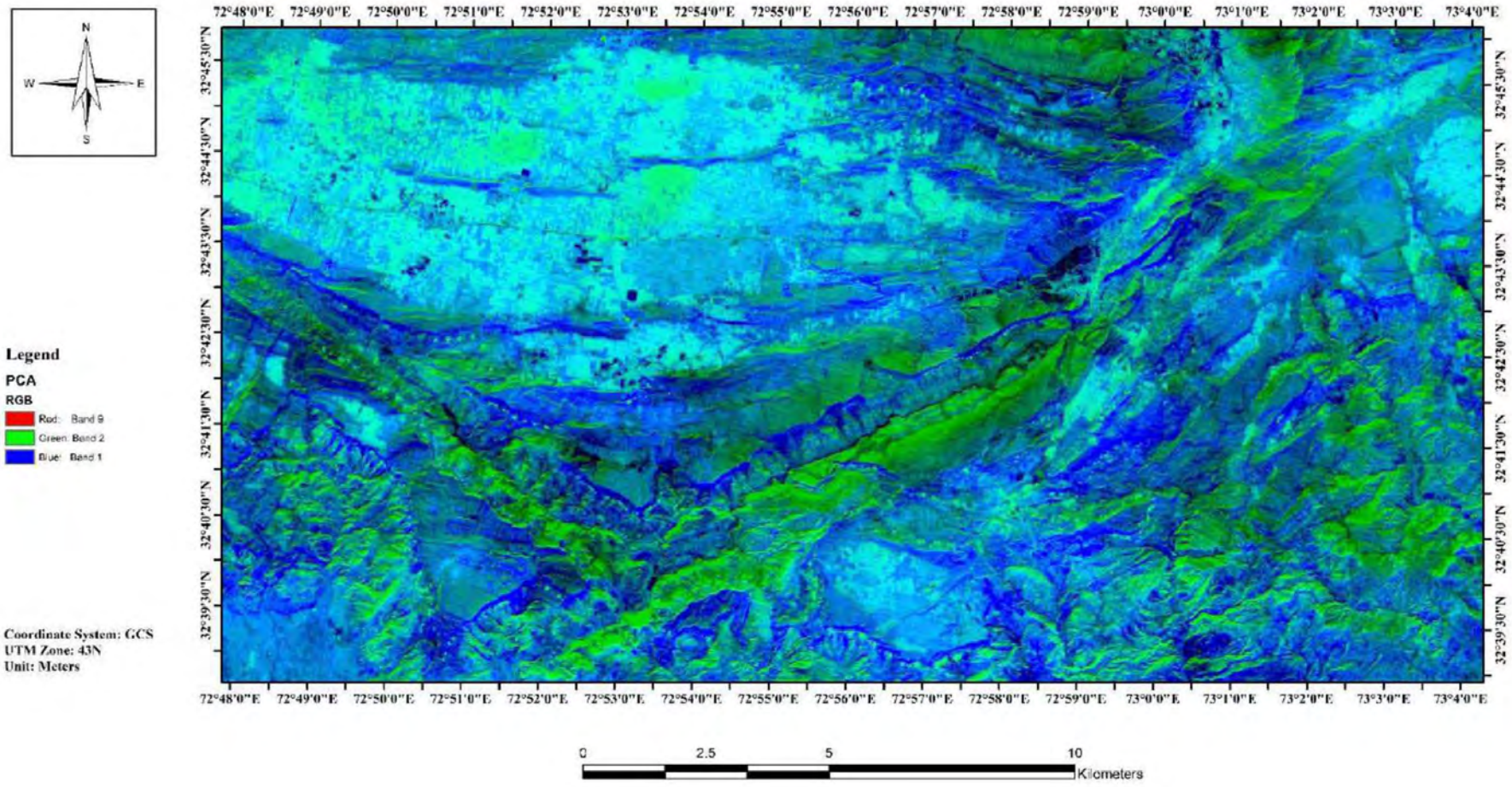

Figure 3.5 PCA 9, 2, 1 with RGB false colour composition with the green in the image representing segregated laterite beds classified in ENVI 5.3 and map prepared in ArcMap 10.4.

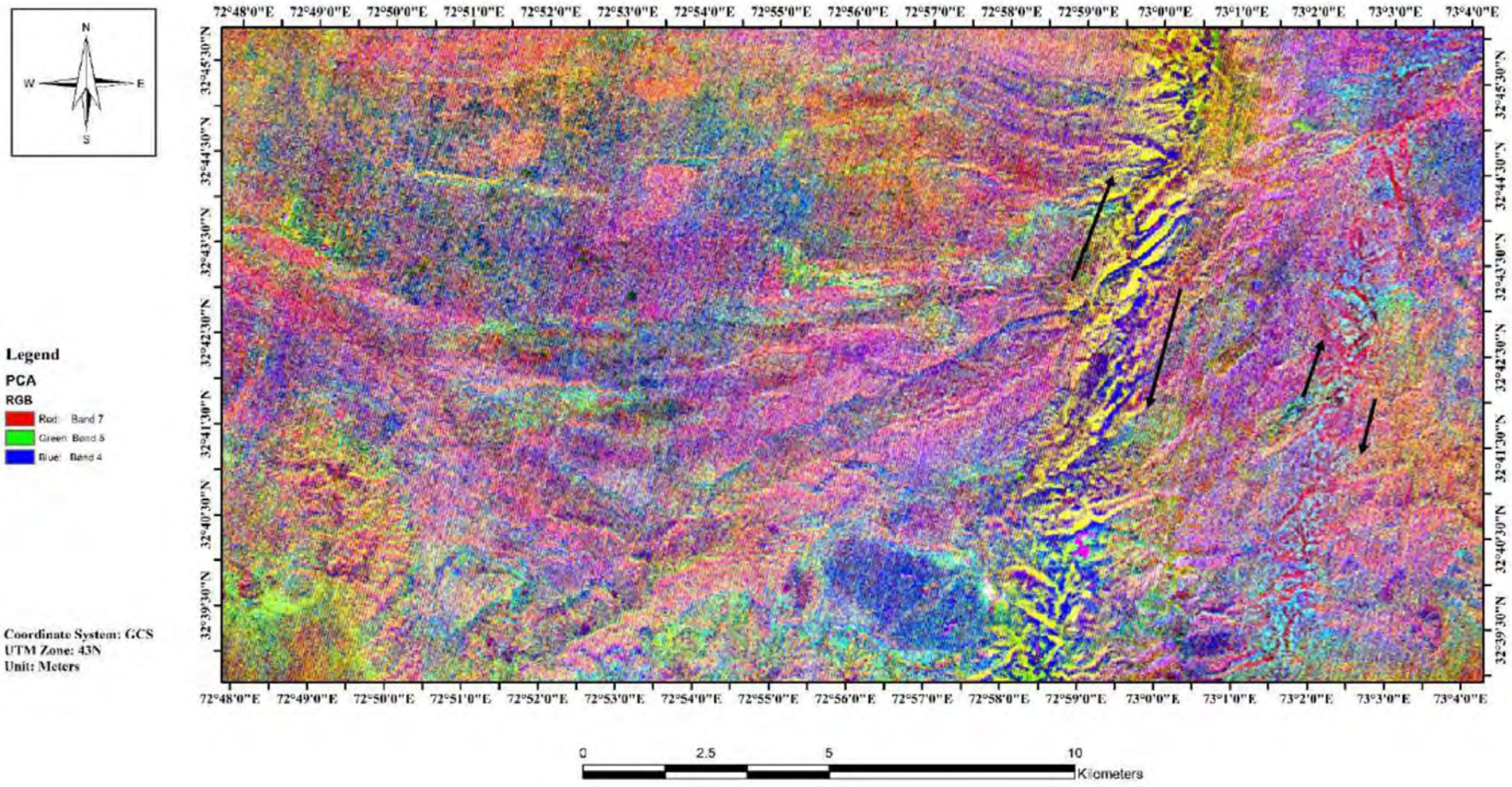

Figure 3.6 PCA 7, 5, 4 with RGB false colour composite able to delineate left lateral strike slips with arrows marking the movement of the strike slip fault in subsurface classified in ENVI 5.3 and map prepared in ArcMap 10.4.

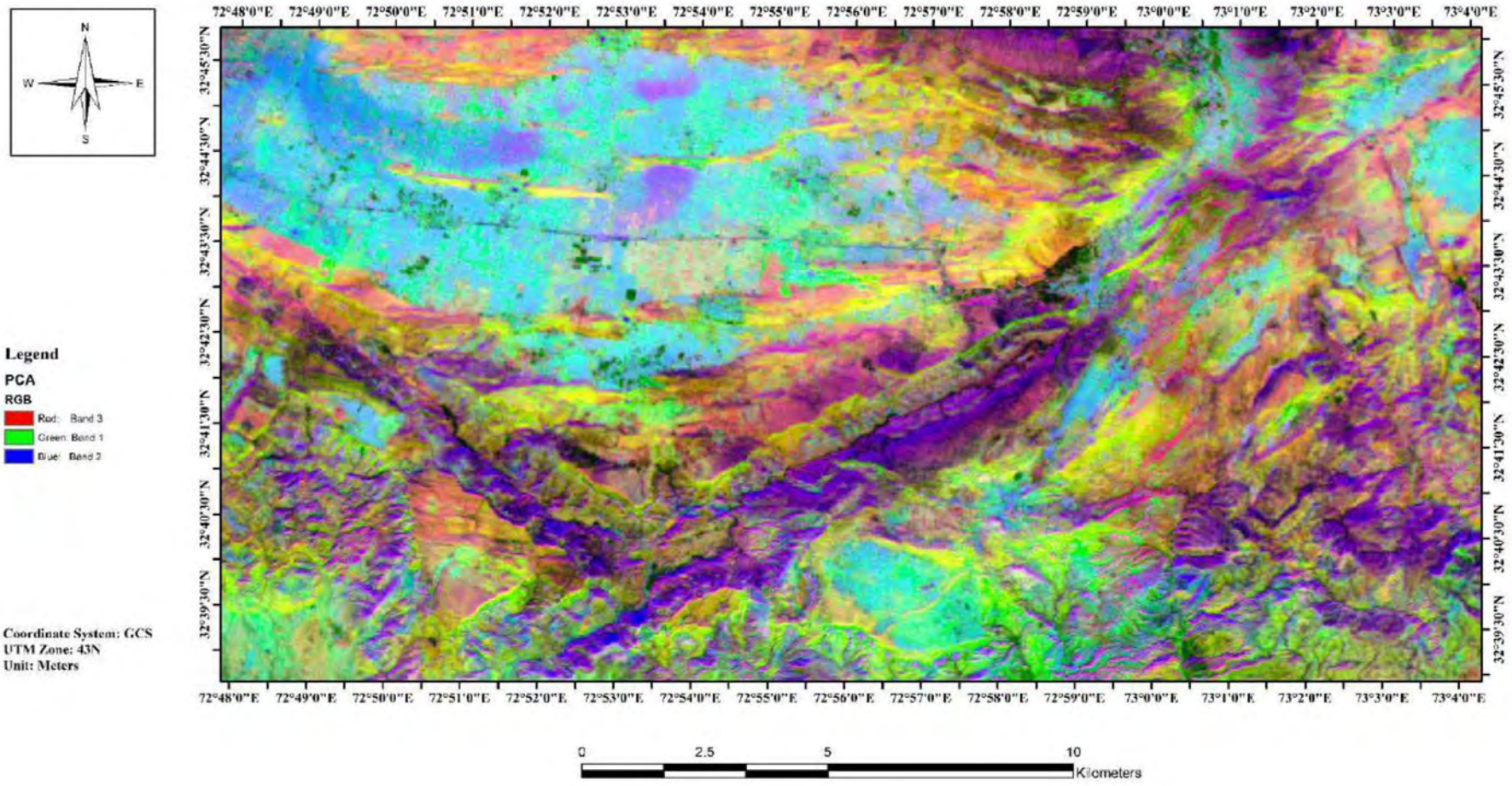

Figure 3.7 PCA 3, 1, 2 with RGB false colour composition with the green hue representing Eocene carbonates, parrot green to yellow hues representing sandstone, sky blue to turquoise hue representing clays, purple to pink hue representing laterite beds classified in ENVI 5.3 and map prepared in ArcMap 10.4.

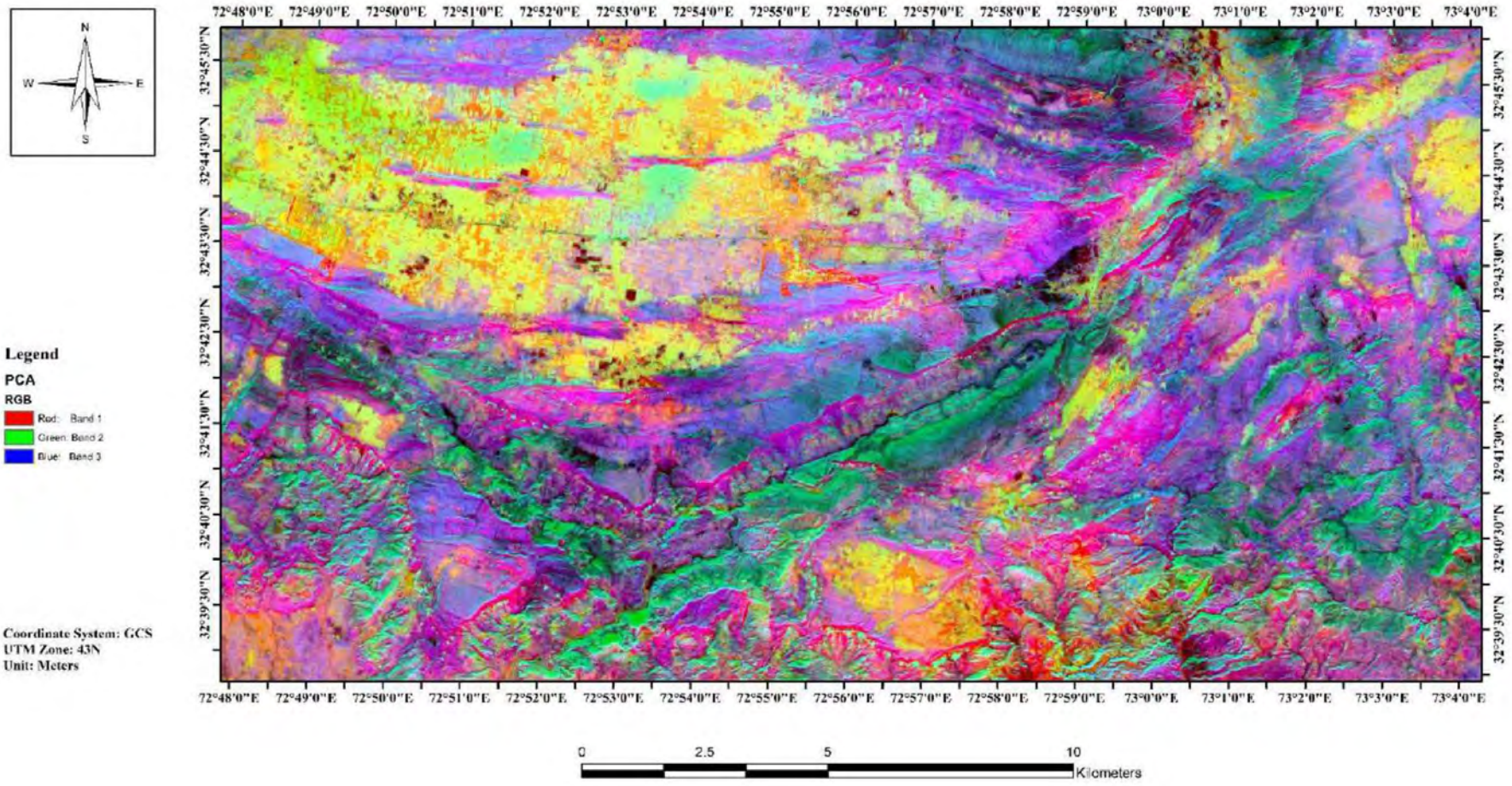

Figure 3.8 PCA 1, 2, 3 with RGB false colour composite showing yellow colours most dominant in areas of clay minerals, with the pink colours dominant of Eocene carbonates exposed in the area. The light green colour being the most vivid in areas of laterite exposure classified in ENVI 5.3 and map prepared in ArcMap 10.4.

3.8.2 BR

BR combinations were similarly utilized to study the lithological setup in the area, with the first combination of the band ratio in the VNIR and SWIR spectrum shown below in Figure 3.9, with the false colour composite of RGB assigned with the BR combination of 5/3+1/2, 4/5, 7/5 respectively. The 5/3+1/2 band ratio was assigned the red channel, 4/5 the green channel and 7/5 the blue channel. The BR were calculated, and layer stacked with the same pattern and classified RGB, in which the clay minerals of the area can be seen in hues of pink and purple, with the laterite deposition in light green, while hues of yellow and orange representing the iron oxide present in the laterite beds of Figure 3.9, while the advanced mineral mapping of the band ratios with applied threshold marked kalonite deposits with umber brown colour, laterite beds with slate blue colour and Fe_2O_3 deposits with red colour, and can be seen below in Figure 3.10 with the threshold and confidence percentage of the band ratios given below in Table 3.

Table 3 Calculated threshold and confidence accuracy percentages utilized in advanced mineral mapping maps using VNIR & SWIR bands.

Band Ratios	**Minimum**	**Maximum**	**Mean**	**Standard Deviation**	**Threshold**	**Confidence**
5/3+1/2	0	255	93	41	216	98%
4/5	0	255	136	65	201	92%
7/5	0	255	151	60	211	92%

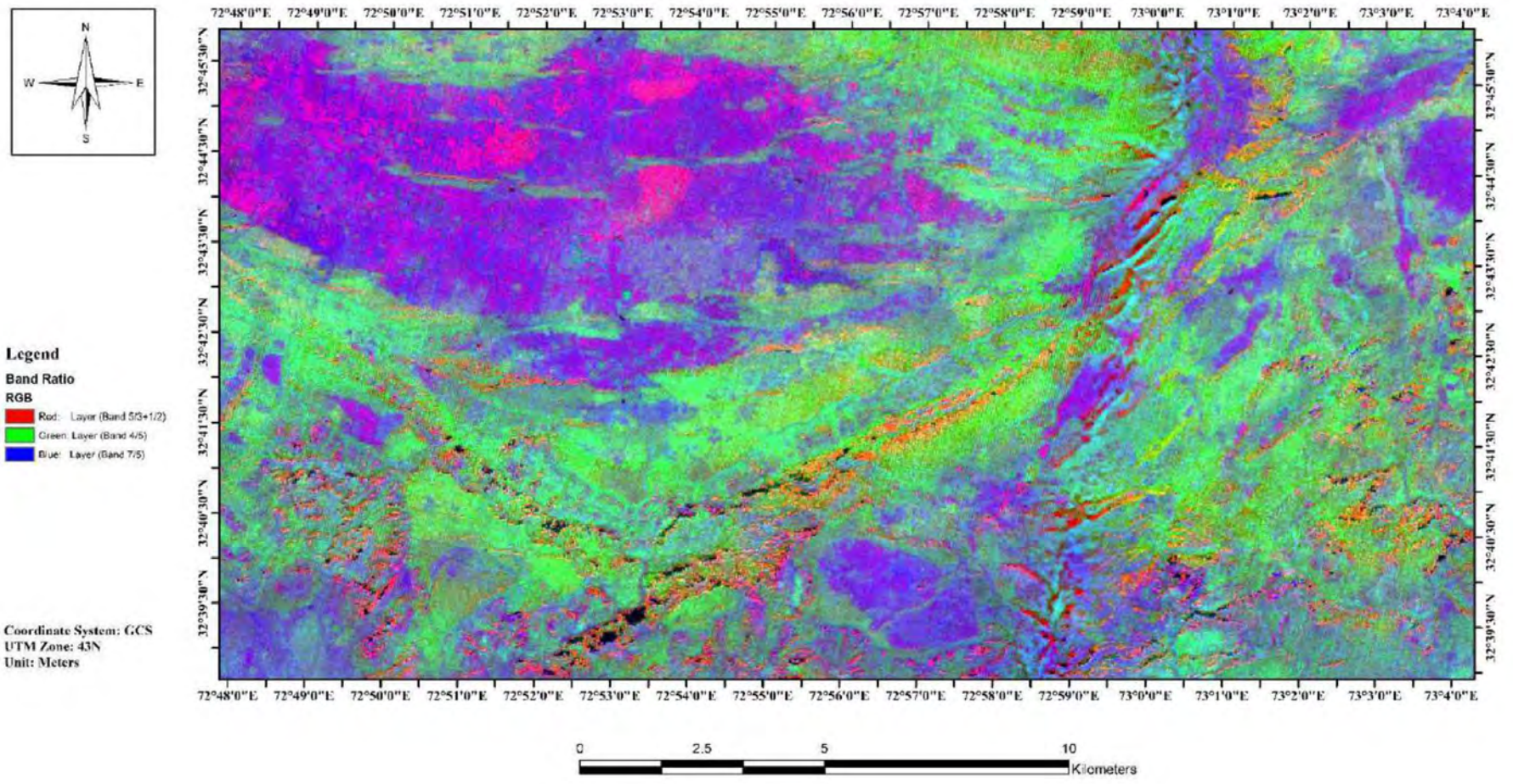

Figure 3.9 Band Ratio image of the study area with false color composite RGB applied on 5/3+1/2 as iron oxide, 4/5 as laterite and 7/5 kalonite classified in ENVI 5.3 and map prepared in ArcMap 10.4.

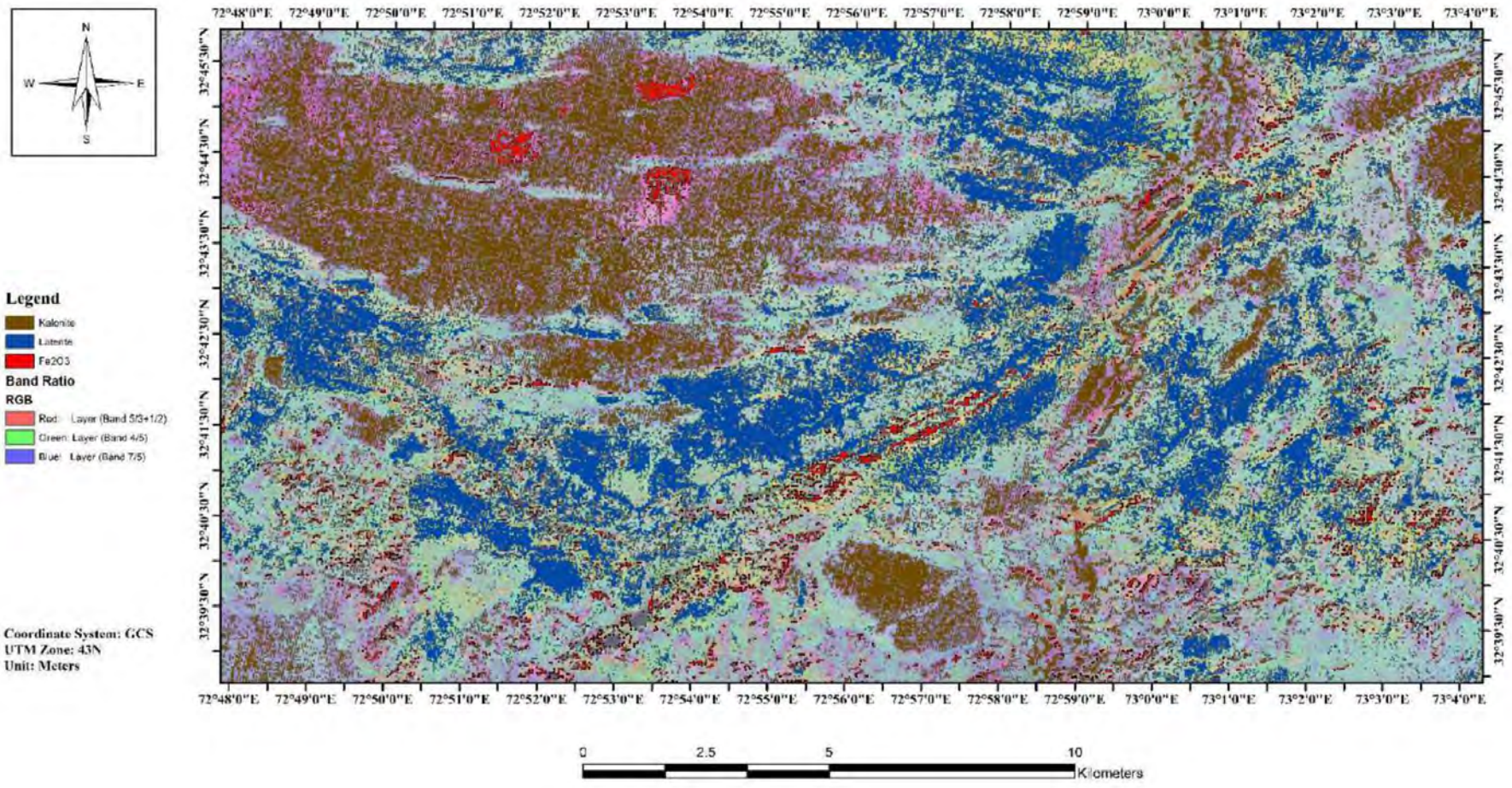

Figure 3.10 Advanced mineral map prepared of the band ratios with iron oxide displayed in red, laterite in slate blue, and kalonite in umber brown classified in ENVI 5.3 and map prepared in ArcMap 10.4.

3.9 TIR

One of the techniques was also applied on the TIR bands to get some more accurate information on the two major deposits present in the area namely carbonates and sandstone bodies. It is to be noted that the spatial resolution of the TIR bands is 90m.

3.9.1 BR

This was the second BR combination that was utilized with the TIR bands for studying lithological setup of the area, with false colour composite of RGB utilized with the band combinations of 14/12 and 13/14 calculated and layer stacked. The resolution of TIR bands being 90m was not much visually aesthetic with the image result as shown below in Figure 3.11, but the red colour assigned to BR 14/12, blue colour assigned to BR 13/14 and green colour assigned to zero band the image marked the sandstones with red while the Eocene carbonates with light blue colour. Advanced mineral mapping was once again carried out with the density threshold applied on the band combinations showed the quartz in yellow scattered above the red bodies marked as sandstone while the dark green colour associated to the carbonates scattered mostly on the light blue colours and can be seen below in Figure 3.12 and the advanced mineral mapping of with confidence percentage and threshold shown below in Table 4.

Table 4 Calculated threshold and confidence accuracy percentages utilized in advanced mineral mapping maps utilizing band ratios of TIR bands.

Band Ratios	Minimum	Maximum	Mean	Standard Deviation	Threshold	Confidence
14/12	0	255	129	59.7	248.4	95%
13/14	0	255	134	59.4	252	95%

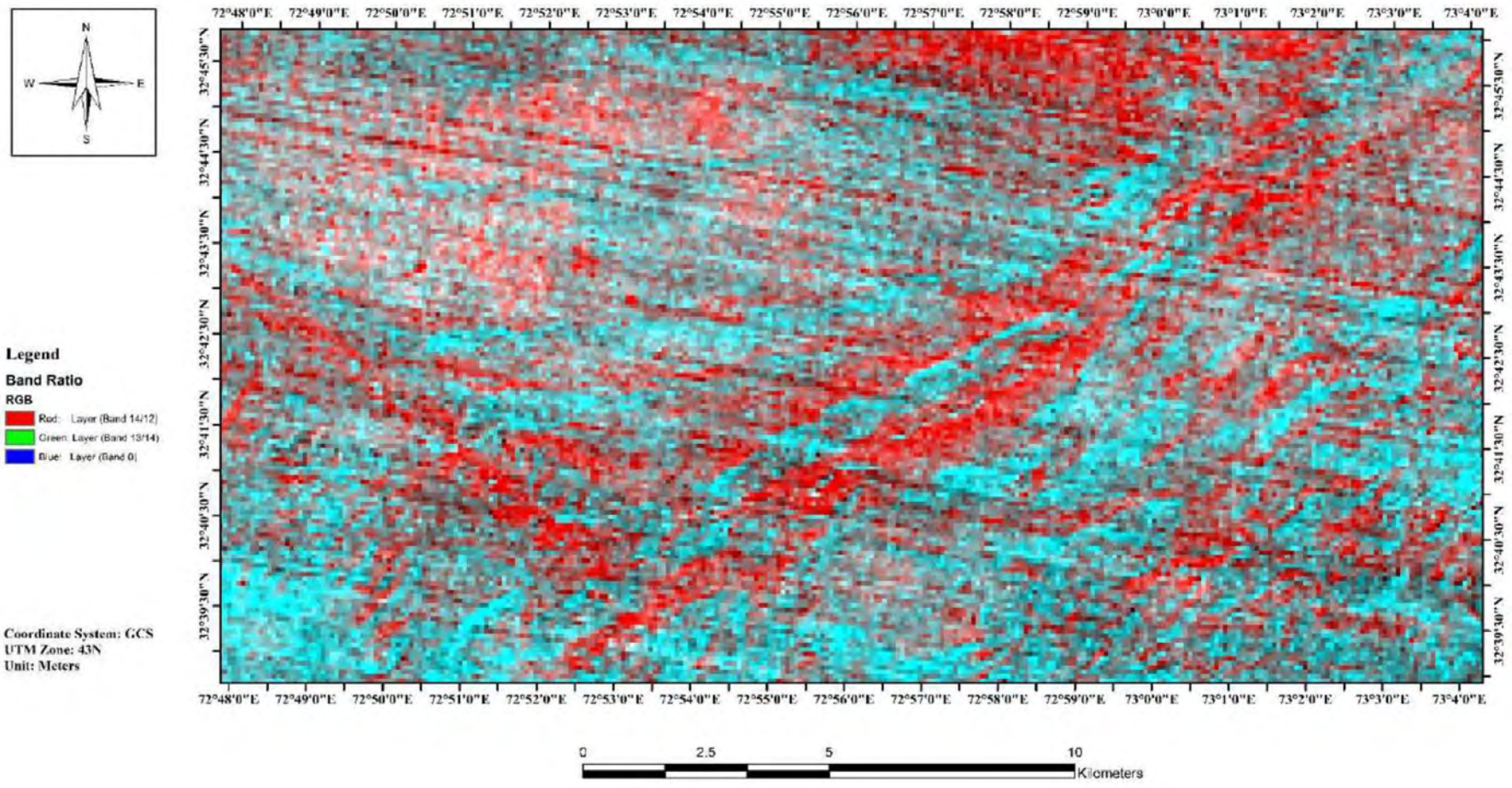

Figure 3.11 Band Ratio image of the study area with false colour composite RGB applied on 14/12 as sandstones and 13/14 as carbonates, classified in ENVI 5.3 and map prepared in ArcMap 10.4.

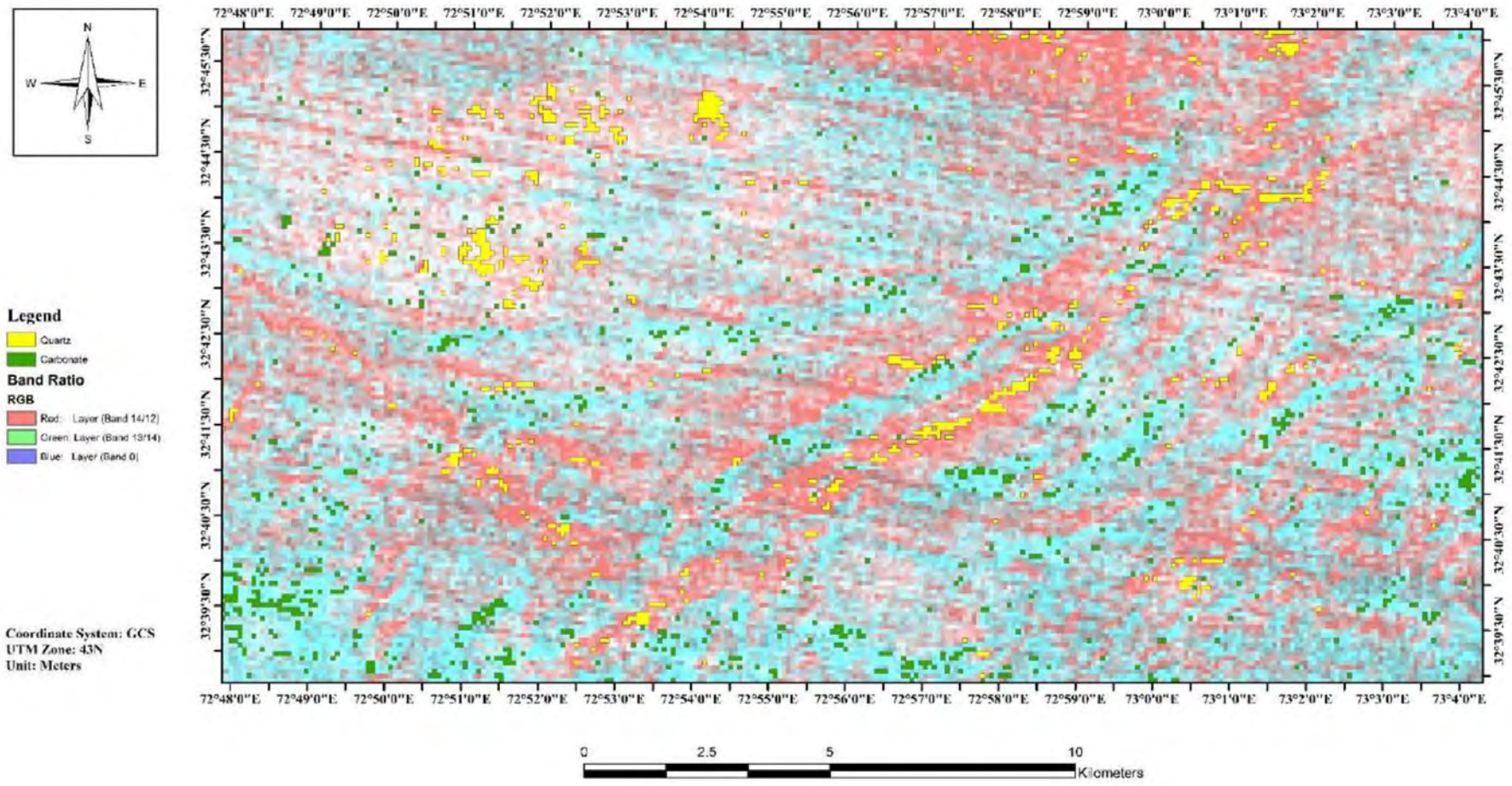

Figure 3.12 Advanced mineral map prepared of the band ratios with sandstone bodies in yellow and carbonates with dark green classified in ENVI 5.3 and map prepared in ArcMap 10.4.

3.10 Accuracy Assessment

When assessing the results of remote sensing interpretation ground control data is a key point that helps in classifying the interpretation accurate or not, but a statistical approach in remote sensing and GIS is accuracy assessment, which statistically helps in mapping the location, distribution of the resources and helps in understanding and analysing its interactions, that is a resourceful method for finding further suitable locations and planning actions for future events. To achieve this accuracy assessment thematic accuracy method was incorporated in the study.

There are two types of accuracy assessment techniques considered: Non-Site-Specific Accuracy evaluation and Site-Specific Accuracy evaluation, with the first technique just deems the total area of classes to quantify and the position of the points is not considered, and the latter considers both the total area of classes and the setting of the points (Martin et al., 2012). With geological samples and magnetic data later recorded of the study area, the sit-specific accuracy assessment was considered for this study.

In terms of geography and development in the areas, the approach of Confusion Matrix was employed with the aid of ENVI software, where Confusion Matrix demonstrated the reliability of the classification result simply by contrasting the classification result to ground factual data (Jensen et al., 1984). The Confusion matrix for each class displays the Kappa coefficient, errors of omissions (these are the left out of class percentage pixels), overall accuracy, errors of commission (those percentage of pixels that are in excess class), user and producer accuracy.

The Kappa Coefficient (K) shown below in Equation (5) is a gauge of precision of classification, which is computed with the sum of confusion matrix diagonals ($\sum_{i=1}^{k} n_{ii}$) being multiplied by the total number of pixels that are found in all ground truth classes (N) and then subtracting the sum of ground truth pixels in a class times the sum of the classified pixels in that class summed over all classes ($\sum_{i=1}^{k} n_{i+} \, X \, n_{+i}$), and dividing by the total number of pixels squared minus the sum of the ground truth pixels in the class times the sum of the classified pixels in that class summed over all classes (2013 ENVI help).

$$K = \frac{N \sum_{i=1}^{k} n_{ii} - \sum_{i=1}^{k} n_{i+} \, X \, n_{+i}}{N^2 - \sum_{i=1}^{k} n_{i+} \, X \, n_{+i}}, \quad (5)$$

Calculation of accuracy level can be achieved as shown in Equation (6), when the number of correctly classified pixels are added and then divided by the total number of pixels, where the true

class of pixels is defined by the region of interest (ROI) or even the ground truth image. Pixels accurately categorized can be located along diagonal of confusion matrix table, which displays the number of pixels categorized into the proper ground truth class. The total amount of pixels across all ground truth categories (2013 ENVI help)

$$O\ A = \frac{\sum_{i=1}^{k} n_{ii}}{N}. \quad (6)$$

In this regard ($\sum_{i=1}^{k} n_{ii}$) is sum of diagonal elements and (N) the total number of pixels.

With 12 points selected on the field containing the location of the points i.e., latitude and longitude, with detail of lithology of the point, these datasets were used for accuracy assessment, below in Table 5 gives the accuracy assessment of the classification techniques used in the study.

Table 5 Site specific accuracy assessment displaying result percentages and Kappa Coefficient of the techniques incorporated.

Classification Techniques VNIR & SWIR Bands	**Band Combination**	**Overall Accuracy Percentage**	**Kappa Coefficient**
BR	**5/3+1/2, 4/5, 7/5**	**73.78%**	**0.7956**
PCA	**9, 2, 1** **7, 5, 4** **3, 1, 2** **1, 2, 3**	**71.90%**	**0.7785**
Original Image		**67.88%**	**0.4853**

CHAPTER 04

APPLICATION OF MAGNETIC METHOD

4.1 Introduction

Geophysics can be termed as science that applies physical and mathematical methods for subsurface studies. It is dependent on the aims and purposes of the parameter estimation research with the aim of magnetic survey to detect and describe parts of the Earth's crust with abnormal magnetizations (Joshua et al., 2017).

Magnetic surveying consists of the following:

- At predefined sites, the terrestrial magnetic field is measured.
- Adjusting measurements to account for diurnal variations.
- Comparison of resultant values of field with expected vale at each measurement station.
- Calculation of the estimated depths from Earth’s surface to magnetic anomaly source.

There are various minerals containing iron and nickel that exhibit ferromagnetism, therefore rocks bearing these elements have significant magnetization and produce considerable local magnetic fields as a result (Nwankwo et al., 2007). The non-destructive technology has a wide range of applications in geo - environmental investigations, including the detection of voids, near-surface faults, igneous dikes, and subsurface ferromagnetic objects (Weymouth, 1986). Magnetic field fluctuations can be used to calculate anomaly depth, geometries, and magnetic susceptibility. Magnetic anomaly maps are useful in assisting geological interpretations (Joshua et al., 2017).

The International Geomagnetic Reference Field is regarded to be the theoretical undisturbed value of the magnetic field at any point on the Earth's surface (IGRF). This formula is used to remove magnetic variations attributable to this theoretical field from the magnetic data, leaving us with residual magnetic anomaly data. As a result, a magnetic anomaly is described as the variation between the observed Earth magnetic field and the expected magnetic field as from International Geomagnetic Reference Field (Lowrie, 2007). Although an alternative procedure suitable for small surveys exist wherein the regional field is approximated by a linear trend and then subtracted from the final field value for each measurement point. Trend Analysis is the term given to this procedure. (Kearey et al., 2002).

Surficial exploration for mineral exploration and exploitation is considered as part of the first and second phase of any study, which is utilized geologically and through remote sensing techniques. With the case study identified of the presence of ferrous laterite beds nearby the village of Ratuchah the third phase of the study was utilized to identify these ferrous laterite beds in the subsurface, that were delineated on the surface. The technique chosen for this case study was the passive magnetic technique, due to presence of metallic minerals it was considered as the most plausible technique which would give the magnetic susceptibility of the variations in the laterite beds in the subsurface.

4.2 Survey Planning

Preliminary planning is necessary for any geophysical work to facilitate field operations and resolve any challenges that may occur during the survey. The key objective of the planning is not only to save time and money, but also to enhance data quality and acquire as much information as possible. Consideration in the sequence of surveying pattern, data collection, and processing procedure allows us to improve data signal-to-noise ratio, which is ultimately essential in the final interpretation of any geophysical survey.

4.3 Survey Design

To conduct our geophysical investigation, we first demarcated the study area most accessible with the help of Google Earth Pro, based on the results of the data interpreted through remote sensing. Survey design demands detailed examination of the subject at hand because it has a substantial impact both on geophysical strategy employed for the kind of survey, like as ground survey, airborne survey, or down hole. The survey plan for geophysical surveys ought to have uniform geophysical data coverage across the region of interest. Depending on the severity of the case study and location, a grid or profiling pattern is employed in terrestrial magnetic surveys. Careful consideration of the survey area, a fishnet grid was developed with the help of ArcMap 10.4, with a station interval of 100m and a profile distance also of 100m, with the length of profiles reaching up to 2.5km and were laid in traverse of the Ratuchah village. A total of 325 stations were established on which magnetic readings were taken, with Figure 4.1 displaying below the profiles designed on study area.

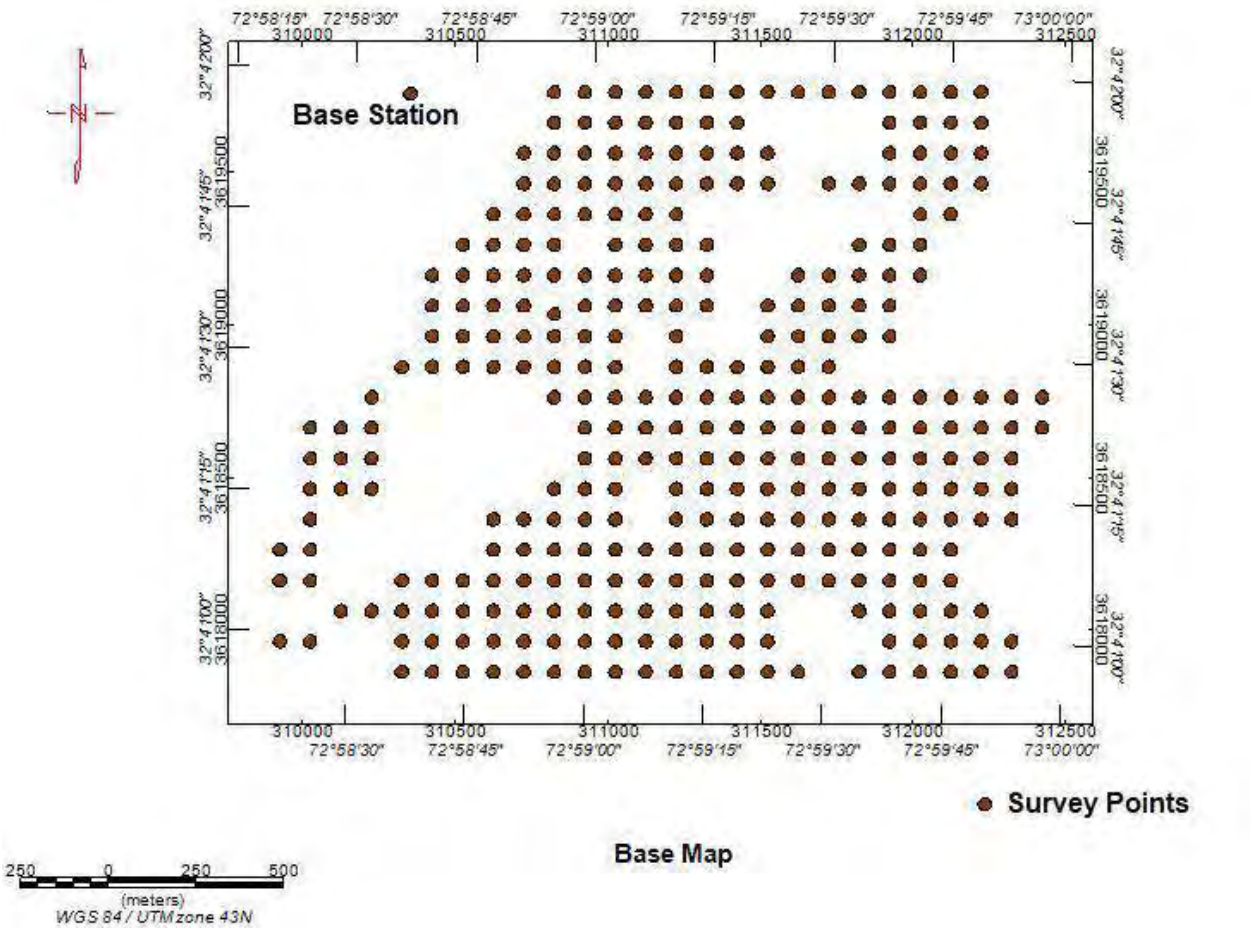

Figure 4.1 Magnetic data acquisition base map of the study area showing the survey stations and the base station that were acquired near Ratuchah, with grid prepared in ArcMap 10.4 and base map prepared in Oasis Montaj.

4.4 Instrumentation

The instrumentation utilized to conduct the geophysical investigation in the area are as follows:

4.4.1 Global Positioning System (GPS)

Magellan triton is a GPS with preprogrammed POIs, a visual compass screen, 3-meter accuracy, and a robust and water-resistant SiRF star3 chipset. It was utilized to discover the field stations by submitting the design survey coordinates & altitude of each field, and the base station was obtained in the field with the use of a Magellan Triton GPS, which can be seen in Figure 4.2.

Figure 4.2 Magellan Triton 400 handheld GPS on which coordinates were stored and utilized in navigation towards the survey points.

4.4.2 Magnetometer

Geometrics' G-856 portable man-carried proton procession magnetometer and a "base station" magnetometer have been used to measure the magnetic intensity of established stations. This is a hand-held instrument featuring simple push-button operation and a built-in digital memory which retains over 5000 readings. It has an average resolution of 0.1 gamma and absolute precision of one gamma, that is constrained by remanent magnetism inside the sensor and crystal oscillator accuracy. It offers an 1800 gamma/meter gradient tolerance. The instrument was calibrated at the created base station by setting the clock, inserting the Julian date, and adjusting the instrument based upon that magnetism of the research region from an internationally accepted Total Magnetic Intensity map. Figure 4.3 depicts the image of instrument used.

Figure 4.3 Geometrics G-856 Proton Precision Magnetometer which was used to acquire field data.

4.5 Field Observation

Magnetic data was acquired in the middle of November 2021, where an auxiliary base station was setup with UTM coordinates of 31120 eastings (X) and 3619838 northings (Y) and the magnetic

data was measured by setting up a magnetometer at the base and the other for field observations, for which field data was acquired for 4 days which can be seen in Table 6 given in Appendix.

The observed magnetic raw data had to be then reduced to base station level with the application of different corrections of universal magnetic formulae. Following ate the correction which were then applied on the magnetic data to generate the anomalies.

- Diurnal Correction
- Normal/Latitude Correction

With the corrections applied and magnetic anomalies generated the reduced magnetic data would then be utilized in the process by Geosoft Oasis Montaj software to generate total magnetic intensity maps, and vertical derivative to observe the placement of the laterite beds and the subsurface geological structures effecting the placement of the laterite beds.

4.6 Reduction of Magnetic Data

4.6.1 Diurnal Correction

These are induced by UV radiation and charged particles emitted by the sun, which ionize the upper atmosphere, creating a change in the magnetic field at the earth's surface. These periodic fluctuations in the intensity of the earth's magnetic field must be compensated for by applying diurnal correction to each observation made during the survey. Normally, diurnal variation has a daily period and an amplitude averaging of about gammas. This can sometimes reach an amplitude of 100 gammas; thus, they must be considered to safeguard the signal from such noisy effects.

The utilization of diurnal variation, as in this example, necessitates the simultaneous employment of two magnetometers, one at the base station and one in the field. Following the same technique, one device was permanently installed at the base station, which recorded continuous fluctuations every 10 minutes. The data from the base station was plotted against time to show the behavior of the diurnal variation about the base station.

These continuous base measurements observed in the vicinity plainly suggest that the external field's general behavior was quite smooth. The first step in applying the diurnal correction was to link the measurement to a certain zero time at a defined reference.

Each field measurement was timed, and the measured difference in intensity was adjusted by adding or subtracting the departing amount noted from the base curve at the time of field readings.

4.6.2 Normal/Latitude Correction

Because the magnetic field varies with geographical location, the normal correction is used when surveying a vast area. The earth behaves like a huge magnet, with the core of the earth resembling a dipole. The amplitude and direction of the Earth's uniform magnetic field have been seen to shift as one move from one location to another. When the geological formations are minor, and the survey is undertaken across a greater area. Because these variations produce inaccuracies, the field data must be corrected. Because the geological features in a tiny area are quite large, there is no need to apply this correctio for such a minor effect. The normal correction is negative towards the north pole and positive towards the equator or south pole as the overall intensity increases from the equator to the north pole. It is possible to compute it using isomagnetic charts. The normal values can be selected from these charts at any latitude, and the variation in magnetic intensity per mile can be estimated by interpolation between latitudes in the studied area.

4.7 Interpretation of Data

The magnetic approach is dependent on a dipolar field as opposed to a monopolar gravitational field, with magnetic traces being the sum of both attracted and repulsive forces, which confuses the interpretation cycle. In this scenario, the dipolar structure of the magnetism causes magnetic data anomalies to be much more susceptible to depth than gravity anomalies.

Gravity estimations are centered on variations in the linear (depth), while the magnetic procedure includes a variety of estimations for comprehension ranging from simple total field anomaly (normal circumstance) to vector, slope, and tensor segments obtained with appropriately situated sensors worked on the ground, from satellite, airborne, or data acquired at sea on ships.

With the collected information and calculated models of anomalous sources created, residual anomalies are generated using enhancement methods, which are applied on the anomalous data. The qualitative procedure entails the setup of remnant anomalies in contour or picture design in terms of variability through: (1) magnitude that resemble the transmission of magnetization aspects pertaining to depositional and structural variability; and (2) wavenumber usually to isolate the shallow depth, high frequency influences from the more enormously sourced, low frequency impacts; however, textural changes in the distribution of rocks of shifting attractive polarization lithologies are also considered; (3) steep gradients that identify geological junctions,

lineaments, faults, or other geologic constraints; and (4) directional patterns that detect geologic unit and structure strike.

Depending on the process's goals, quantitative interpretation might take several shapes. It may consist solely of estimating depths to sources, interpreting subsurface magnetic subunits from such a magnetic profile using either forward or reverse demonstration processes, or a mixture of both, and isolation of remanent anomalies interpreted by modelling.

4.8 Qualitative Interpretation

4.8.1 Total Magnetic Intensity Map (TMI)

Utilizing the minimum curvature technique, a magnetic anomaly map of the acquired data was thus generated, with automated contours of the software as depicted in the Figure 4.4, below displaying the range of the total magnetic intensity map lying in -131.7 nT to 212.3 nT, in which the TMI map was able to clearly distinguish the ferromagnetic laterite beds prominent in the northeast to southwest direction with visible increase of the bodies in the southwest direction. The high magnetic anomalies are characteristic of the laterite bodies that are referred to as mudstones in the outcrop geology and are usually hematite rich bodies as observed through geochemical analysis of sample data. The low values observed in the western portion of the study area shows low magnetic susceptibility due to the presence of Eocene carbonate exposures in contrast to the hematite containing mudstones having high magnetic susceptibility.

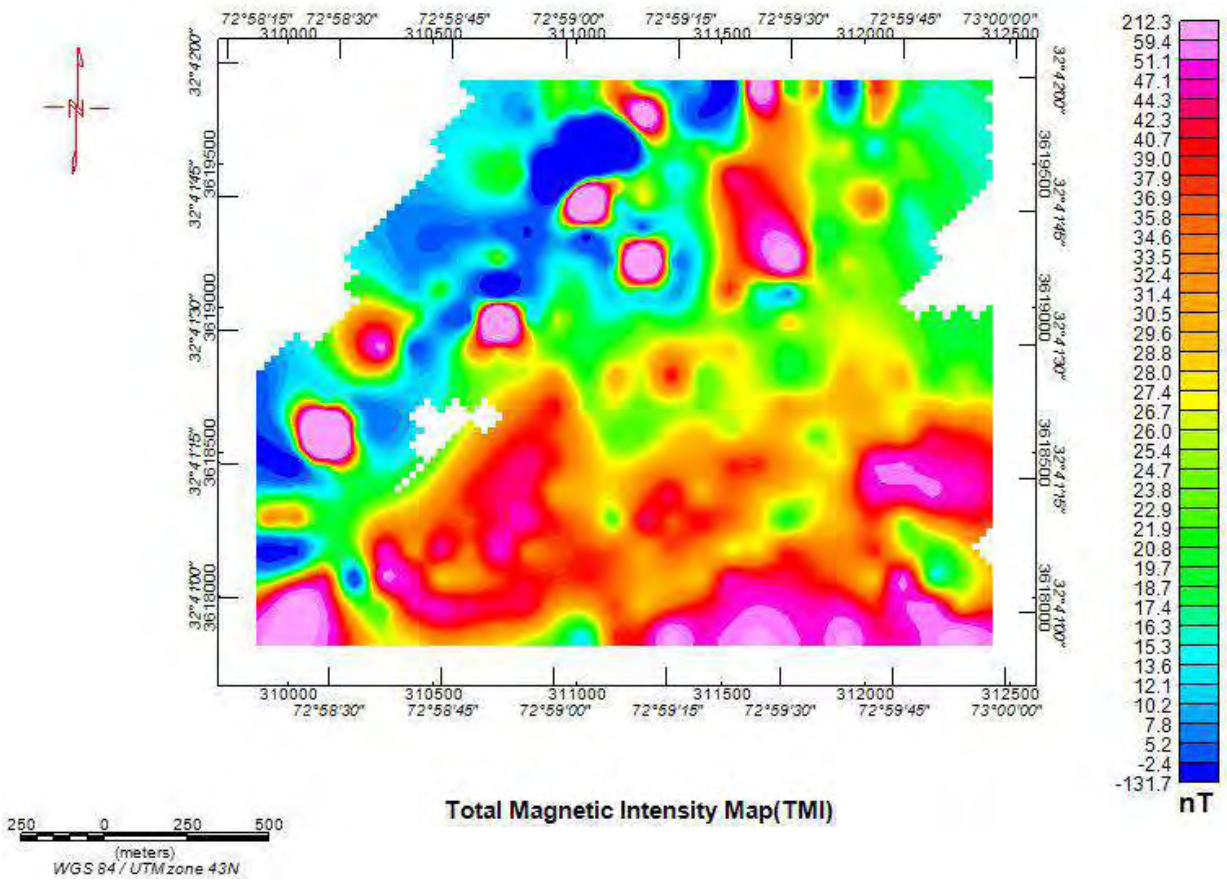

Figure 4.4 Total magnetic intensity map of the study area in the region of Eastern Salt Range of Pakistan in the vicinity of villages Ratuchah and Pidh.

4.8.2 Regional-Residual Separation

Anomalies of relevance are commonly superimposed on a local field by sources larger than the size of the research or too significant to be regarded of interest. In the current situation, it is critical to carry out regional-residual separation, which is a necessary first step in data comprehension. Indeed, this challenge has now been brought closer by utilizing easy graphical procedures (physically selecting data points to correspond to a smooth regional field) or by utilizing various mathematical methods to attain regional field. Initially, the graphical methodology was limited on collapsing profile information and, less importantly, gridded information. The earliest nongraphic approach used a territorial field defined as the normal of field estimations over a sphere of a specified radius, with the remainder being the difference between the observed an incentive at the central axis of the circle and this normal proposed using 2D direct frequency filtering. To address the problem, a strategy employing a synchronized channel for segregating the residue field from regional field was demonstrated. Pawlowski and Hansen suggested an approach based on

frequency Wiener filtering that used the range of detected information and looked for clear discontinuities in between low and high frequency regions of the range to extract relevant regional and residual fields (Pawlowski & Hansen, 1990; Guspí & Introcaso, 2000).

Match filtering and Weiner filters share common characteristics with conventional direct band-pass channels, but they have the distinct advantage of being suited for a variety of geologic models.

To generate the residual map of the study area using the magnetic data a generalized Equation (7) was utilized which is the following:

$$G_o = G_1 - G_2. \quad (7)$$

where, G_o denotes the residual map, with G_1 as the grid of the total magnetic intensity map, and G_2 is the interval of 500m applied as the upward continuation grid.

4.8.3 Upward Continuation

On (or near) the initial observation surface, anomalous magnetic knowledge is deciphered. However, there are times when it is necessary to migrate (or progress) the data to a different surface for analysis or to seem differently in respect to some other data collection. To construct a regional magnetic map of the area, an upward continuation of 500m was applied to the magnetic anomaly map.

4.8.4 Regional Map

With the understanding that potential anomalous map is really an aggregation of impacts of different subsurface structures occurring at diverse profundities, it is essential to remove those regional effects from potential anomaly in order to isolate the discrete impacts in the study area. The regional map defines the deep underground structure, or the basement. An upwards continuation technique, as previously mentioned, is used to construct the regional map. With the range of magnetic susceptibility of the study region being from 7.4 nT to 48.1 nT with a north to south trend, having a low magnetic zone in the northeast, and a high magnetic zone in the southwest as depicted in the Figure 4.5 below.

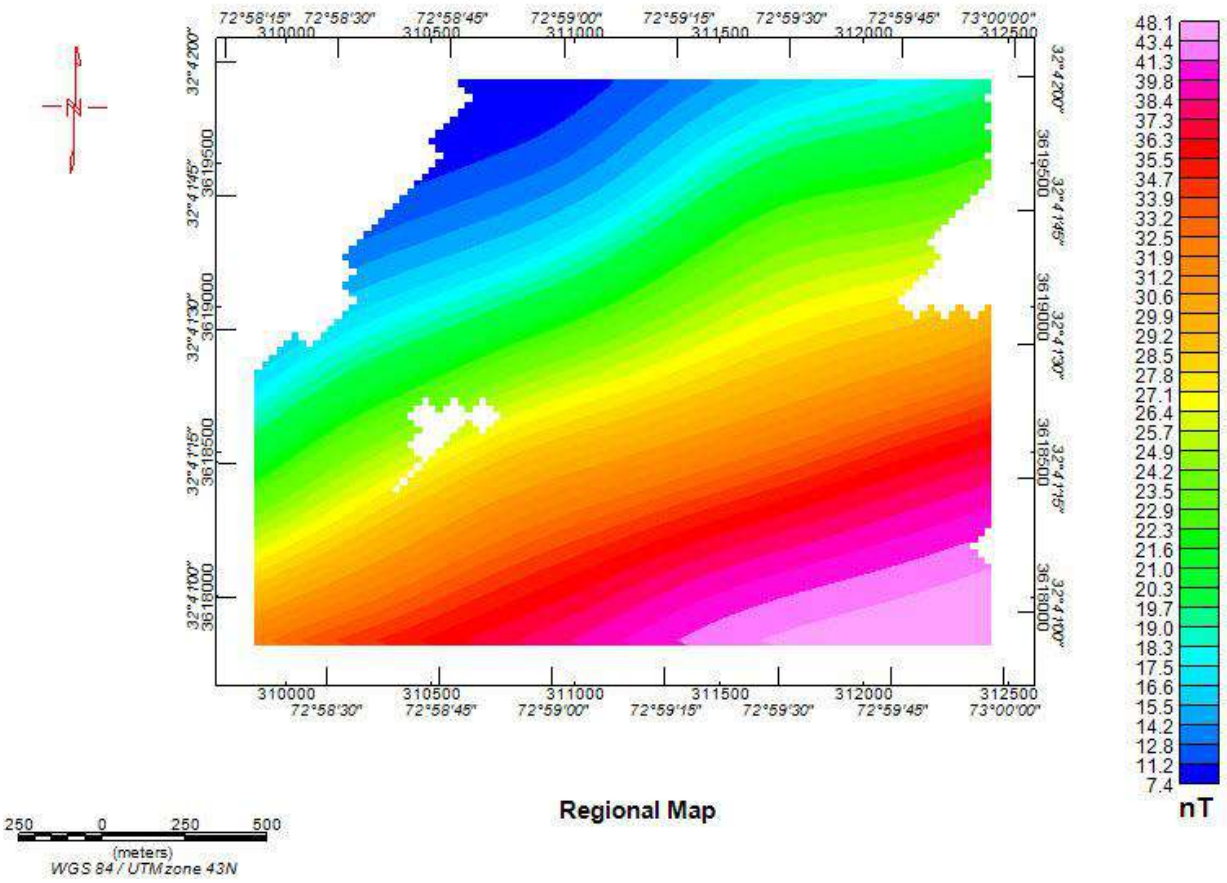

Figure 4.5 Regional total magnetic intensity map of the study region in vicinity of villages Ratuchah and Pidh in the Eastern Salt Range of Pakistan.

4.8.5 Residual Map

Residual map of the study region having a range with the maximum being 190.3 nT and a minimum of -144.6 nT, with enhanced shallow features in prospect to the magnetic susceptibility of rocks in the surrounding. The shallow features prominently show clear structural features along the low magnetic susceptibility region that are visible in the north and follow a trend of northeast to southwest region, directly in correlation to the strike slip fault marked in the PCA 7, 5, and 4. Splays extending to the west and east of the strike slip are marked as S1, S2, and S3 below in Figure 4.6 These features are the result of short wavelength enhancement providing clear image of the shallow feature of the strike slip in the subsurface. The low magnetic susceptibility is also in context to the presence of carbonate rocks in the region, which can be seen below in the Figure 4.6. The higher magnetic susceptibility in the study region displays the ferromagnetic nature of the laterite beds, also since these bodies are found in the mudstones which are hematite rich characteristic of the Patala formation. The low magnetic susceptibility in some areas is simply due

the Eocene carbonates, while medium magnetic susceptibility ranging from -4.6 nT to 2.3 nT is a fact of the clay bodies in the area.

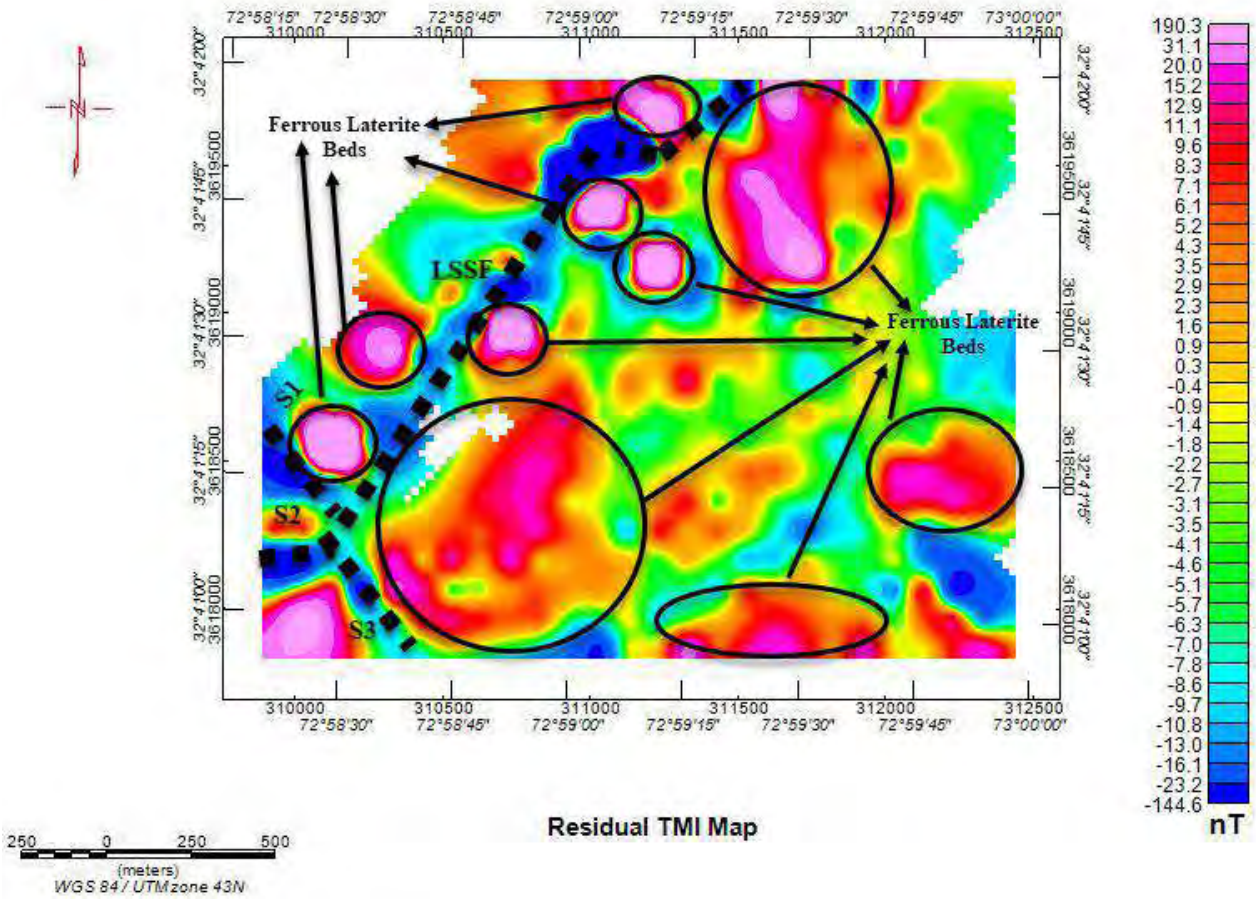

Figure 4.6 Residual total magnetic intensity map separated from the regional of the research area in vicinity of villages Ratuchah and Pidh, of Eastern Salt Range of Pakistan.

4.8.6 Reduction to Pole (RTP)

Removing magnetic data's influence on magnetic inclination, i.e., transforming data collected in the inclined Geomagnetic field to how it would have appeared if the magnetic field had been vertical. RTP reduces inclination-induced anomaly asymmetry and detects anomalies above source bodies, assuming that remanent magnetism is minimal in comparison to induced magnetism. It is challenging to accomplish at small magnetic inclinations, therefore reduction to equator is favored. If the magnetization reduction direction is known, the total field magnetic anomaly can be reduced to the pole. RTP analysis done on the residual magnetic anomaly map of the study area with the inclination I, of 51.2 and the declination D, of 22.4 utilizing the calculation of the IGRF. While the residual map does make prominent the shallow features of the subsurface but also comprises

of cultural noise (near surface noise) which has been removed using RTP. Thus, in contrast to the residual TMI map it is observed that RTP map is smoother, and there is a significant improvement in the high magnetic anomalies and the low magnetic anomalies, which can be seen in Figure 4.7 below. The amplitude of the RTP anomalies varies between -153.0 nT and 221.9 nT, with magnetic high anomalies observed closely on the ferromagnetic laterite bodies, which can be observed due correlating to the geochemical sample locations in the study area, and the low magnetic anomalies over the strike slip and its splays marked as S1, S2, and S3 with their occurrence observed above, and the carbonate successions in the area. RTP analysis was carried out on this magnetic data since the study area falls within the mid-latitude region.

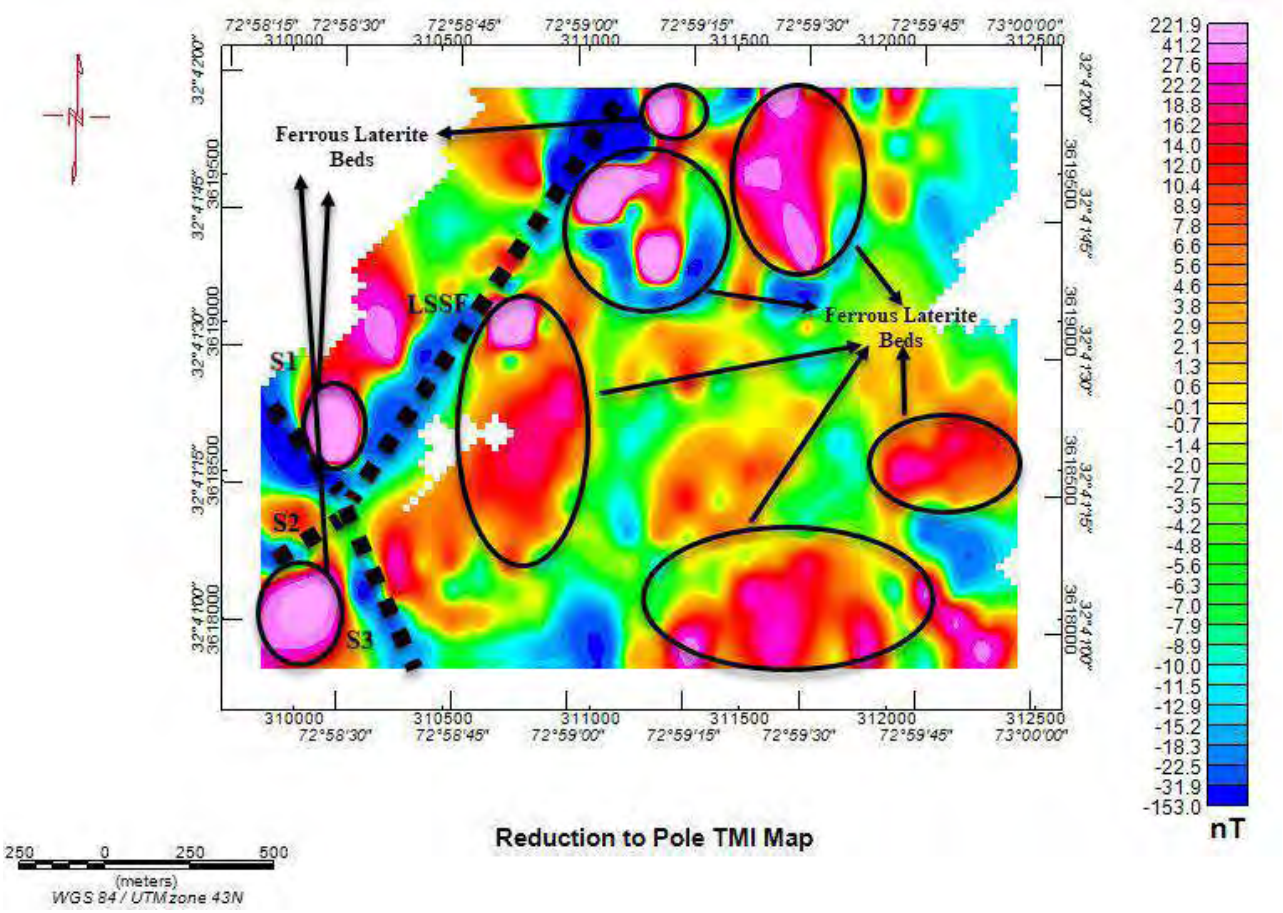

Figure 4.7 Reduction to Pole (RTP) map of the residual total intensity map, with much smoother contours formed over causative anomalies of study area, near vicinity of villages Ratuchah and Pidh of Eastern Salt Range, Pakistan.

4.8.7 First Vertical Derivative

The first vertical derivative amplifies the influence of short-wavelength anomalies and discontinuities while providing a clear resolution of shallow subsurface features. Although it

provides a crisp image of the subsurface features, it has the disadvantage that because it magnifies its short wavelength, data integrity might be substantially compromised by magnifying noise. The magnetic anomalies due to deep sources is reduced by using vertical derivatives.

After enhancement of the shallow subsurface features, which can be seen in the Figure 4.8 information concerning the strike slip feature and its splays are more prominent after the application of the first vertical derivative filter applied on the RTP residual TMI map. The low magnetic anomalies of the range -4.290 nT to -0.127 nT is association also to the carbonate rocks of the Salt Range and the Dil-Jabba thrust to the west. In contrast to both RTP and residual maps more enhanced ferromagnetic anomalies of the laterite beds can be seen in the range of 0.234 nT to 7.344 nT. Another aspect of the filter that can be noticed is the connection of the ferromagnetic laterite beds which was not much visible with the RTP and residual TMI maps.

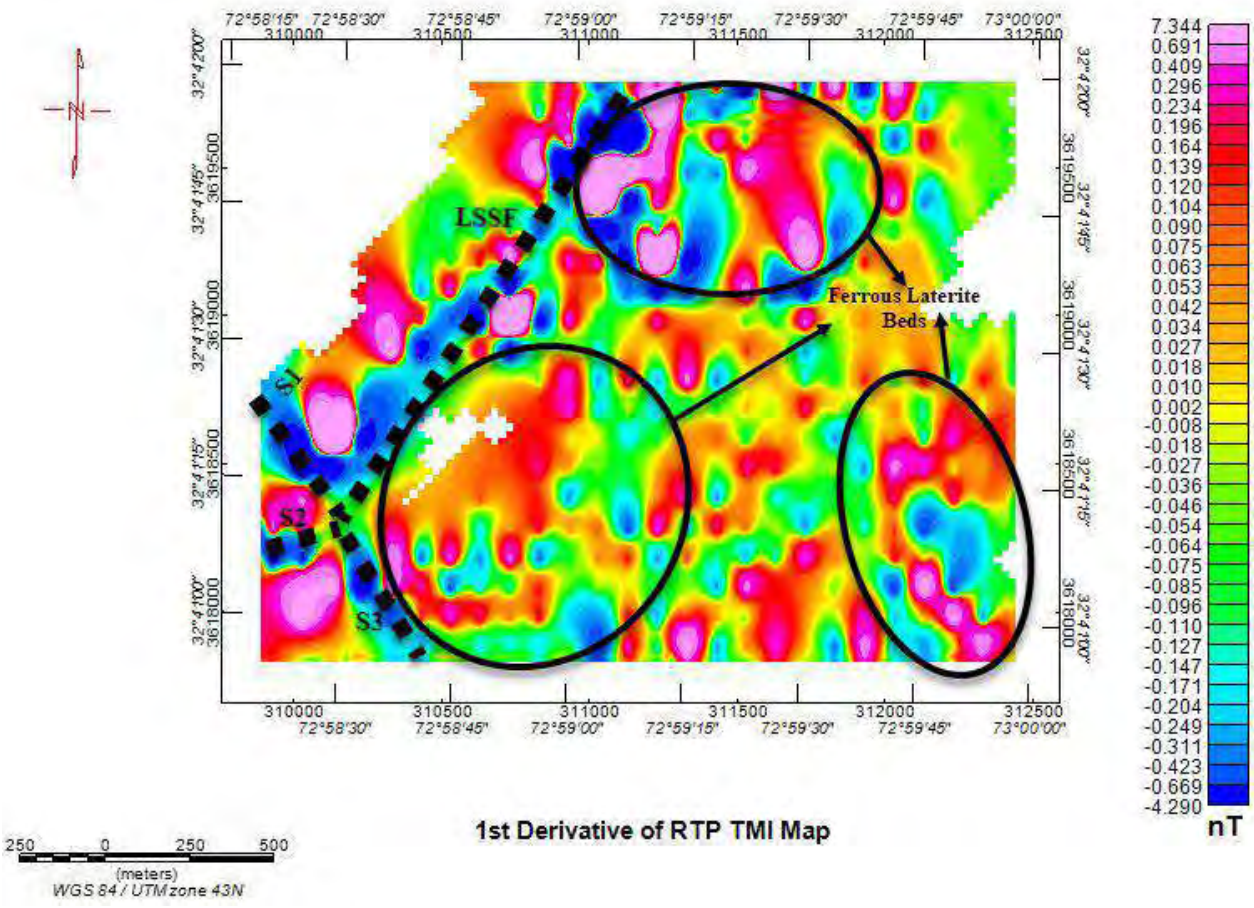

Figure 4.8 First vertical derivative map applied on RTP anomalies that enhances the short wavelength anomalies of the research area, in vicinities of Ratuchah and Pidh of Eastern Salt Range, Pakistan.

4.8.8 Total Horizontal Derivative

This filter emphasizes the effective linear edge structure as a positive maximum, which is frequently related with the existence of faults and contacts. The total horizontal derivative can be expressed in the Equation (8):

$$Total\ Horizontal\ Derivative = \sqrt{\left(\frac{\partial m}{\partial x}\right)^2 + \left(\frac{\partial m}{\partial y}\right)^2}. \quad (8)$$

Here, $\left(\frac{\partial m}{\partial x}\right)^2$ and $\left(\frac{\partial m}{\partial y}\right)^2$ are derivatives of magnetic field in x and y direction, with the gradient being positive always.

The high of total horizontal derivatives typically occurs across the steep gradients of magnetic anomaly relief's slope, indicating cause boundaries, whilst minimum occurs over flat regions, with maxima connected to magnetic susceptibility differences and threshold depth.

4.8.9 Tilt Derivative

Tilt derivative, also known as normalized phase derivative, employs first order derivatives and seems to be a highly successful method for mapping subsurface structural edges, described in Equation (9):

$$Tilt\ Derivative = \tan^{-1}[VDR/THDR]. \quad (9)$$

Here the VDR is referred to as the first vertical derivative and THDR as horizontal derivative. Because of the characteristics of the arctan function, the values must be between ($\pi/2$ and $-\pi/2$), regardless of the frequency and amplitude of the VDR and THDR. This simulates the automatic gain control (AGC) filter that evenly distributes the amplitude result of magnetic anomalies over a grid. This derivative is distinct in that it is independent of density or magnetization, whereas the VDR and THDR are factors of subsurface density or magnetism. As a result, it is an effective technique for detecting subsurface structural boundaries from faint Bouguer or TMI anomalies.

Potent effect of the tilt derivative filter was seen in the data when applied, as it clearly demarcates the high ferromagnetic laterite beds, with clear extensions in contrast to th e first vertical derivative map. The range of the high magnetic anomalies can be seen from 1.013 nT to 1.553 nT, with its edges clearly well defined, present in the northeast with increase in the number of bodies in the southern region and are separated from the low magnetic anomalies present in the area attributed

to the carbonate rocks present in the area. The laterite beds increase in the southwest direction, with a major bed of laterite identified near the village of Pidh. As depicted in the Figure 4.9 below the linear strike slip feature can be seen narrowed down and in continuation in the northeast to southwest direction and its splays in the east and western direction. The advanced mineral mapping that displayed the ferromagnetic exposures on the surface, visible in the tilt derivative filter.

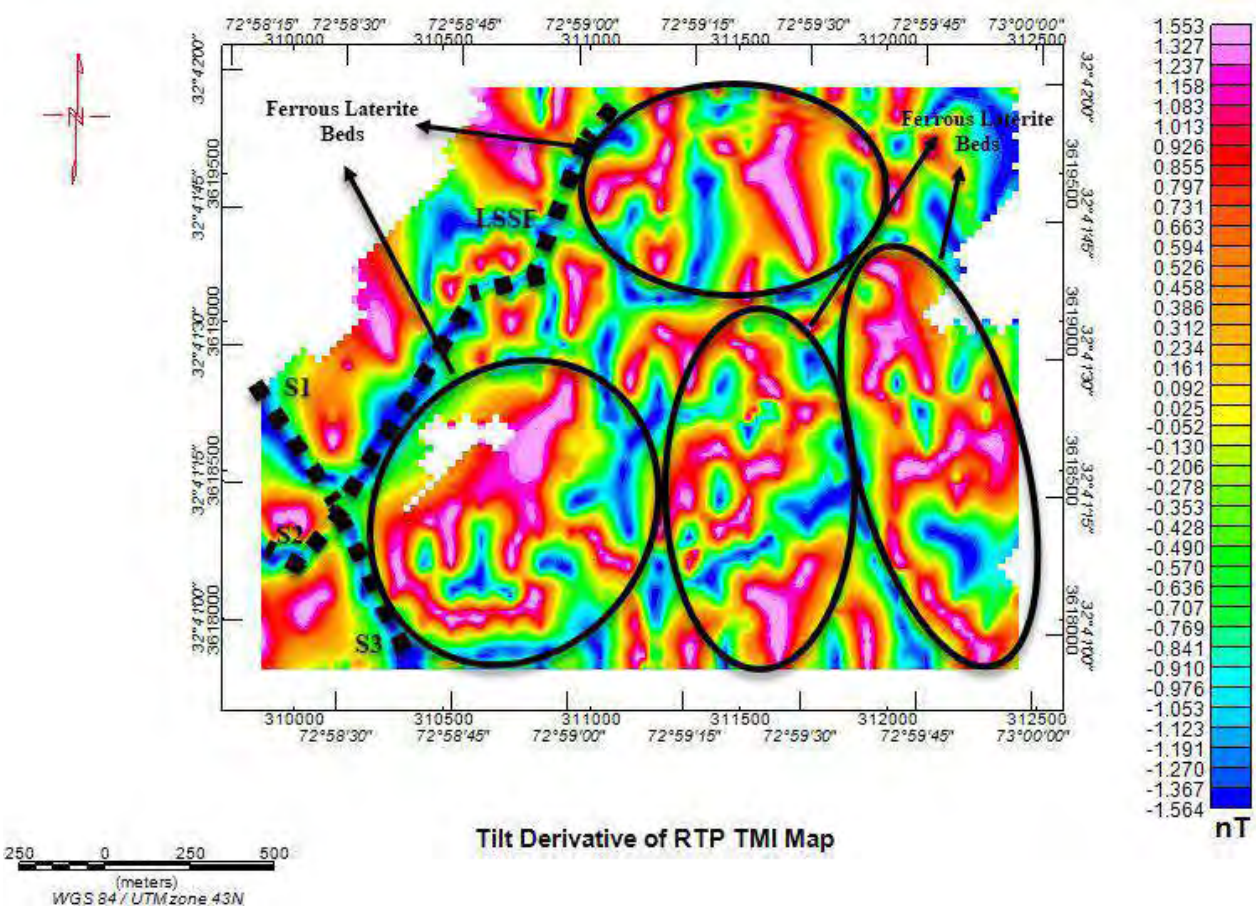

Figure 4.9 Tilt Derivative applied on the study area showing more connection of the ferromagnetic laterite beds and left lateral strike slip fault near vicinity of villages Ratuchah and Pidh, of Eastern Salt Range, Pakistan.

CHAPTER 05

DISCUSSIONS AND CONCLUSIONS

5.1 Discussions

Economic mineral distribution of the ferromagnetic laterite beds near the Thesil of Choah Saidan Shah was to be explored in terms of presence of ferromagnetic laterite bodies using remote sensing data, and its subsurface continuation in the study area through terrestrial magnetic method. The magnetic profiles were placed in the southeast of the visual interpretation of the advanced mineral maps generated from the ASTER data. The acquired magnetic data was correlated with the techniques applied to the ASTER data and the geochemical analysis of the samples collected during the geological field, that helped in establishing the subsurface continuation and identification of the ferromagnetic laterite bodies.

The area is potentially rich with industrial minerals such as limestone, coal, talc, and laterite, with maximum excavation being done by the Pakistan Mineral Development Corporation of the limestone present in the area and of coal by local miners. There has been almost no previous study with regards to mineral content in the zone of interest located on the edge of the Dil-Jabba thrust and the Salt Range thrust that merge in the Potowar plateau. Geochemical analysis was conducted on twelve field samples of the exposed laterite beds. The results showed a high average percentage of quartz of 52.6%, with second most abundance of iron oxide with average percentage of 27.1% and with only average 16.4% of aluminum oxide thus, concluding that the laterite beds are dominant with iron oxide.

At first remote sensing data analysis was applied on a regional scale to the zone of interest, where different techniques were employed in understanding the characteristics of study area. The PCA band combinations segregated the laterite exposures from the surrounding clay, carbonates, and quartz content. PCA analysis also helped in identifying the structural variation in the study area as PCA band combination of 7, 5, and 4 was able to identify the left lateral strike slip presence in the study area. The band ratio technique further refined the results of the specific exposures by identifying laterite, iron oxide and kalonite minerals, with the use of VNIR and SWIR stacked band combinations that were resampled at 30m spatial resolution. Advanced mineral maps were established in which the threshold of the iron oxide presence in the laterite beds was observed and was consequently correlated with the geological samples of the study area. The analysis was

fruitful in observing the ferromagnetic content of the laterite beds of the Hangu Formation, which was segregated from the otherwise characteristically indistinguishable Patala Formation, through geochemical analysis. The samples were then utilized with the ASTER data to create an accuracy assessment of the digital images. The site-specific accuracy evaluation gave higher accuracy percentages of 73.78% for band ratio and 71.90% for the PCA of VNIR and SWIR stacks and a higher Kappa coefficient. The satellite-based analysis in combination with the sample collection helped in locating the most accessible region to conduct ground magnetic survey for laterite bed detection. The generated residual anomalies were in the range of -144.6 nT to 190.3 nT. RTP of the TMI map was able to smoothen out the residual anomalies and the left lateral strike slip with a trend of northeast to southwest direction was clearly observed towards the east. First vertical derivative of the RTP residual TMI map was able to enhance the amplitudes of the ferromagnetic laterite anomalies. The edges of the ferromagnetic laterite bodies present with undulating elevation structure were enhanced with the help of tilt derivative. In the tilt derivative map, the minimum value of the magnetic anomalies of -1.564 nT attributed to the carbonate rocks present in the area and the maximum value of 1.553 nT of the ferromagnetic laterite beds. The left lateral strike slip was also captured with low magnetic susceptibility with the lineament following the direction confirmed through the other applied methods. The advantage of this filter was that no cultural noises were induced in the data.

5.2 Conclusions

The following conclusions were drawn from this study:

- Integrated study of the GIS, geochemical and magnetic depicts not only the structural variation of the Choah Saidan Shah area situated in the Eastern Salt Range, but also the ferromagnetic laterite potential in the area.
- Geochemical analysis of the field samples in the study area, showed abundant minerals of quartz, with hematite being the second most abundant mineral in the mudstones of Paleocene rocks.
- PCA analysis of the region segregates the lithologies and the demarcation of left lateral strike slips in the study area with band combination 7, 5 and 4 very clearly with the false color composites of RGB.

- Band ratio technique evidently shows the presence of ferromagnetic content in the laterite prone region, with the advanced mineral mapping marking the maximum threshold on the surface reflectance maps.
- The surficial marking of the length of the lateritic beds showed reserves amounting up to 0.41 million tonnes, present in the study area.
- Magnetic low anomalies confirmed the northeast to southwest trending strike slip identified by PCA.
- Enhancement of short wavelength residual anomalies by first vertical derivative further confirms presence of left lateral strike slip and the corresponding high anomalies of the laterite beds that are hematite rich.
- Tilt derivative filter was able to point out the edges of the structures containing ferromagnetic laterite beds with a range of 1.013 nT to 1.553 nT, and further resolved left lateral strike slip with its splays trending in the eastern and western direction.

References

Abbas, S.H., and Hassan, M., 1985, Laterite of Karuli-Choa Sidan Shah area, Salt Range, Jhelum District, Punjab, Pakistan: Lahore, Geological Survey of Pakistan Information Release 237, 12 p.

Adam, E. A., & Agib, A. R. A. (2001). Compressed stabilised earth block manufacture in Sudan. *France, Paris: Printed by Graphoprint for UNESCO*.

Adams, J. B., & Gillespie, A. R. (2006). *Remote sensing of landscapes with spectral images: A physical modeling approach*. Cambridge University Press.

Ajaka, E.O. and Oyathelemi, E.O. (2010). Suggesting Areas for Detailed Investigation of Mineral Occrrences in Nigeria for National Resource Database. ARPN Jour. Of Engr. And Applied Sciences, 5 (11), 27-39.

Al-Jabri, K., & Shoukry, H. (2014). Use of nano-structured waste materials for improving mechanical, physical and structural properties of cement mortar. *Construction and Building Materials*, *73*, 636–644. https://doi.org/10.1016/j.conbuildmat.2014.10.004

Amosun, J. O., Alagbe, O. A., Fagbemigun, T. S., Sanuade, O. A., & Olaseeni, O. G. (2020). Imaging lateritic bauxite bearing zones in Ekiti, southwestern Nigeria, using magnetic and electrical resistivity tomography techniques. *SN Applied Sciences*, *2*(12). https://doi.org/10.1007/s42452-020-03785-w

Ashraf, M., Qureshi, W.M., and Faruqi, F.A., 1972, Preliminary studies on the economic geology of bauxite/laterite deposits, Katha area, Salt Range, Punjab, Pakistan: Punjab University Geological Bulletin 9, p. 43–53.

Bachar, M., Azzouz, L., Rabehi, M., & Mezghiche, B. (2015). Characterization of a stabilized earth concrete and the effect of incorporation of aggregates of Cork on its thermo-mechanical properties: Experimental study and modeling. *Construction and Building Materials*, *74*, 259–267. https://doi.org/10.1016/j.conbuildmat.2014.09.106

Baker, D. M. (1988). *Balanced structural cross section of the central Salt Range and Potwar Plateau of Pakistan, Shortening and overthrust deformation*. D. M. Baker, "balanced structural cross section of the Central Salt Range and potwar plateau of pakistan- shortening and over thrust deformation," M.S. thesis, Oregon State University, Corvallis, 1988, 120p. - references - scientific research publishing. Retrieved from https://www.scirp.org/(S(lz5mqp453edsnp55rrgjct55.))/reference/referencespapers.aspx?referenceid=939616

Baker, D. M., Lillie, R. J., Yeats, R. S., Johnson, G. D., Yousuf, M., & Zamin, A. S. (1988). Development of the himalayan frontal thrust zone: Salt Range, Pakistan. *Geology*, *16*(1), 3. https://doi.org/10.1130/0091-7613(1988)016<0003:dothft>2.3.co;2

Bamousa, A. O. (2011). Infracambrian superimposed tectonics in the late Proterozoic units of Mount Ablah area, Southern Asir Terrane, Arabian Shield, Saudi Arabia. *Arabian Journal of Geosciences, Springer*, *6*(6), 2035–2044. https://doi.org/10.1007/s12517-011-0490-5

Bromley, R.G., and Frey, R.W., 1974, Redescription of the trace fossil *Gyrolithes* and taxonomic evaluation of *Thalassinoides*, *Ophiomorpha* and *Spongeliomorpha*: Bulletin of the Geological Society of Denmark, v. 23, p. 311–335.

Burbank, D. W., & Raynolds, R. G. (1988). Stratigraphic keys to the timing of thrusting in terrestrial foreland basins: Applications to the northwestern himalaya. *Frontiers in Sedimentary Geology*, 331–351. https://doi.org/10.1007/978-1-4612-3788-4_17

Butler, R. W. H., Coward, M. P., Harwood, G. M., & Knipe, R. J. (1987). Salt control on thrust geometry, structural style, and gravitational collapse along the Himalayan Mountain front in the salt range of northern Pakistan. *Dynamical Geology of Salt and Related Structures*, 339–418. https://doi.org/10.1016/b978-0-12-444170-5.50013-0

Carper, W., Kiefer, R., & Lillesand, T. (1987). Enhancement of SPOT image resolution using an Intensity-Hue-Saturation transformation. In *American Society for Photogrammetry and Remote Sensing and ACSM, Fall Convention, Reno, NV* (pp. 348-361).

Chakraborty, R., Champatiray, P. K., Sengar, V., & Sharma, R. U. (2015). *Mineral identification by band ratios and feature oriented principal component selection techniques in the Bhukia region, Rajasthan*. Retrieved August 20, 2021, from https://aars.org/proceeding/ACRS2017/ID_753_1652/1411.pdf

Coates, D. R. (1985). Mineral Resources. In *Geology and society*. essay, Springer US.

Cooley, T., Anderson, G. P., Felde, G. W., Hoke, M. L., Ratkowski, A. J., Chetwynd, J. H., Gardner, J. A., Adler-Golden, S. M., Matthew, M. W., Berk, A., Bernstein, L. S., Acharya, P. K., Miller, D., & Lewis, P. (2002). Flaash, a Modtran4-based atmospheric correction algorithm, its application and validation. *IEEE International Geoscience and Remote Sensing Symposium*, *3*, 1414–1418. https://doi.org/10.1109/igarss.2002.1026134

Crósta, A. P., De Souza Filho, C. R., Azevedo, F., & Brodie, C. (2003). Targeting key alteration minerals in epithermal deposits in Patagonia, Argentina, using Aster imagery and principal component analysis. *International Journal of Remote Sensing*, *24*(21), 4233–4240. https://doi.org/10.1080/0143116031000152291

Crósta, A., & Moore, J. (1989). Enhancement of LANDSAT Thematic Mapper Imagery for Residual Soil Mapping in SW Minas Gerais State Brazil: A Prospecting Case History in Greenstone Belt Terrain. *Seventh Thematic Conference on Remote Sensing for Exploration Geology*. Calgary, Alberta, Canada.

Gad, S., & Kusky, T. (2007). Aster spectral ratioing for lithological mapping in the Arabian–nubian shield, the neoproterozoic wadi kid area, Sinai, Egypt. *Gondwana Research*, *11*(3), 326–335. https://doi.org/10.1016/j.gr.2006.02.010

Galloway, W. E., & Hobday, D. K. (1983). Terrigenous clastic depositional systems. *New York, Springer-Verlag*, 423. https://doi.org/10.1007/978-1-4684-0170-7

Gee, E. R., & Gee, D. G. (1989). Overview of the geology and structure of the salt range, with observations on related areas of northern Pakistan. *Tectonics of the Western Himalayas*, 95–112. https://doi.org/10.1130/spe232-p95

Gee, E.R., 1980, Pakistan geological Salt Range series: Directorate of Overseas Surveys, United Kingdom, for the Government of Pakistan, and Geological Survey of Pakistan, 6 sheets, scale 1:50,000.

Ghauri, A.A.K., 1977, The study of structures having directional properties and delineation of provenance with help of heavy mineral analysis in the Khewra Sandstone: Bulletin of the Centre of Excellence in Geology, University of Peshawar, v. 9–10, no. 1, p. 79–84.

Ghauri, A.A.K., 1979, Sedimentary structures of the Jutana Dolomite and the Baghanwala Formation: Bulletin of the Centre of Excellence in Geology, University of Peshawar, v. 12, no. 1, p. 1–10.

Guha, A., Singh, V. K., Parveen, R., Kumar, K. V., Jeyaseelan, A. T., & Dhanamjaya Rao, E. N. (2013). Analysis of Aster data for mapping bauxite rich pockets within high altitude lateritic bauxite, Jharkhand, India. *International Journal of Applied Earth Observation and Geoinformation*, *21*, 184–194. https://doi.org/10.1016/j.jag.2012.08.003

Guspí, F., & Introcaso, B. (2000). A sparse spectrum technique for gridding and separating potential field anomalies. *Geophysics*, *65*(4), 1154–1161. https://doi.org/10.1190/1.1444808

Hassan, M., 1985, Investigations for coal in Sammewala mine area, central Salt Range, Punjab, Pakistan: Lahore, Geological Survey of Pakistan Information Release 232, 8 p.

Houben, H., & Guillaud, H. (1994). *de l'article/du chapitre Earth construction. A comprehensive guide*. distributeur Craterre-Eag.

Jaumé, S. C., & Lillie, R. J. (1988). Mechanics of the salt range-potwar plateau, Pakistan: A fold-and-thrust belt underlain by evaporites. *Tectonics*, *7*(1), 57–71. https://doi.org/10.1029/tc007i001p00057

Jensen, J. R., Christensen, E. J., & Sharitz, R. (1984). Nontidal wetland mapping in South Carolina using Airborne Multispectral Scanner Data. *Remote Sensing of Environment*, *16*(1), 1–12. https://doi.org/10.1016/0034-4257(84)90023-3

Joshua, E. O., Layade, G. O., Akinboboye, V. B., & Adeyemi, S. A. (2017). Magnetic mineral exploration using ground magnetic survey data of TAJIMI area, Lokoja. *Global Journal of Pure and Applied Sciences*, *23*(2), 301. https://doi.org/10.4314/gjpas.v23i2.10

Jurgan, H., Abbas, G., and Mujtaba, M., 1988, Depositional environments and porosity development in lower Eocene limestone formations of the Surghar Range, Salt Range, and Potwar Basin, Pakistan: Hannover, Germany, Bundesanstalt für Geowissenschaften und Rohstoffe Technical Cooperation Project Report, Project 83.2068.1, 80 p.

Jurgan, H., and Abbas, G., 1991, On the Chorgali Formation at the type locality: Pakistan Journal of Hydrocarbon Research, v. 3, no. 1, p. 35–45.

Kahle, A. B., Abrams, M. J., Abbott, E. A., Mouginis-Mark, P. J., & Realmuto, V. J. (1995). Remote Sensing of Mauna Loa. *Mauna Loa Revealed: Structure, Composition, History, and Hazards*, 145–170. https://doi.org/10.1029/gm092p0145

Kalinowski, A., & Oliver, S. (2004). ASTER Mineral Index Processing Manual. *Remote Sensing Applications Geoscience Australia*. http://www.ga.gov.au/imagecache/GA7833.pdf

Kasthurba, A. K., Santhanam, M., & Mathews, M. S. (2007). Investigation of laterite stones for building purpose from Malabar region, Kerala state, SW India – part 1: Field studies and profile characterisation. *Construction and Building Materials*, *21*(1), 73–82. https://doi.org/10.1016/j.conbuildmat.2005.07.006

Kazmi, A. H., & Jan, M. Q. (1997). *Geology and tectonics of Pakistan*. Graphic Publishers.

Kearey, P., Brooks, M., & Hill, I. (2002). An introduction to geophysical exploration (3rd). *Great Britain: Blackwell Science Ltd*.p155-180.

Khan, M.A., and Khan, N.J., 1979, Petrology of the Baghanwala Formation, Khewra Gorge, Khewra, Jhelum District, Punjab, Pakistan: Bulletin of the Centre of Excellence in Geology, University of Peshawar, v. 12, no. 1, p. 11–20.

Kingston, D. R., Dishroon, C. P., & Williams, P. A. (1983). Hydrocarbon plays and global basin classification. *AAPG Bulletin*, *67*. https://doi.org/10.1306/ad46093b-16f7-11d7-8645000102c1865d

Law, B. E., & Hussnain, T. (1989). Measured stratigraphic sections of the Lower Permian Nilawahan Group, Salt Range, Punjab Province, Pakistan. *Open-File Report*. https://doi.org/10.3133/ofr89464

Leathers, M., 1987, Balanced structural cross section of the Salt Range and western Potwar Plateau, Pakistan—Deformation near the strike-slip terminus of an overthrust sheet: Corvallis, Oregon State University, M.S. thesis, 228 p.

Lilisand, K. a. (2008). *Remote Sensing and Image Interpretation* (Sixth ed.). Wiley. pp.524-527

Loughlin, W. P. (1991). Principal component analysis for alteration mapping. *Photogrammetric Engineering and Remote Sensing*, *57*(9), 1163-1169.

Lowrie, W. (2007). Fundamentals of Geophysics. *Cambridge University Press*, 310–324. https://doi.org/10.1017/cbo9780511807107

Makasa, B. (2004). Utilisation and improvement of lateritic gravels in road bases. *International Institute for Aerospace survey and Earth Sciences, Delft*.

Martin, C. F., Krabill, W. B., Manizade, S. S., Russell, R. L., Sonntag, J. G., Swift, R. N., & Yungel, J. K. (2012). *Airborne topographic mapper calibration procedures and accuracy assessment* (No. NASA/TM-2012-215891).

McDougall, J. W. (1988). *Geology and geophysics of the foreland fold-thrust belt of northwestern Pakistan*. Retrieved from https://ir.library.oregonstate.edu/xmlui/bitstream/handle/1957/40024/McDougallJamesW1989.pdf?sequence=1

McDougall, J. W., & Hussain, A. (1991). Fold and thrust propagation in the western himalaya based on a balanced cross section of the Surghar Range and Kohat Plateau, Pakistan (1). *AAPG Bulletin*, *75*. https://doi.org/10.1306/0c9b280d-1710-11d7-8645000102c1865d

McDougall, J. W., & Khan, S. H. (1990). Strike-slip faulting in a foreland fold-thrust belt: The kalabagh fault and western salt range, Pakistan. *Tectonics*, *9*(5), 1061–1075. https://doi.org/10.1029/tc009i005p01061

McFarlane, M.J., 1976, Laterite and landscape: New York, Academic, 151 p.

Medlicott, H.B., 1886, Memorandum on the discussion regarding the boulder-beds of the Salt-range: Records of the Geological Survey of India, v. 19, pt. 2, p. 131–133.

Middlemiss, C.S., 1892, Petrological notes on the boulder-bed of the Salt Range, Punjab: Records of the Geological Survey of India, v. 25, p. 29–35.

Molnar, P., & Tapponnier, P. (1975). Cenozoic tectonics of Asia: Effects of a continental collision: Features of recent continental tectonics in Asia can be interpreted as results of the India-eurasia collision. *Science*, *189*(4201), 419–426. https://doi.org/10.1126/science.189.4201.419

Moslow, T. F. (1984). Depositional models of shelf and shoreline sandstones. *American Association of Petroleum Geologists Continuing Education Course Note*, 102. https://doi.org/10.1306/ce27438

Nwankwo, L. I., Olasehinde, P. I., & Bayewu, O. O. (2007). Depth estimates from a ground magnetic survey across a north- south trending geologic structure in a part of the basement complex terrain of ilorin, west of Central Nigeria. *Global Journal of Pure and Applied Sciences*, *13*(2). https://doi.org/10.4314/gjpas.v13i2.16696

Oyelami, C. A., & Van Rooy, J. L. (2016). A review of the use of lateritic soils in the construction/development of sustainable housing in Africa: A geological perspective. *Journal of African Earth Sciences*, *119*, 226–237. https://doi.org/10.1016/j.jafrearsci.2016.03.018

Pawlowski, R. S., & Hansen, R. O. (1990). Gravity anomaly separation by wiener filtering. *Geophysics*, *55*(5), 539–548. https://doi.org/10.1190/1.1442865

Pennock, E. S., Lillie, R. J., Zaman, A. S. H., & Yousaf, M. (1989). Structural interpretation of seismic reflection data from Eastern Salt Range and Potwar Plateau, Pakistan. *AAPG Bulletin*, *73*. https://doi.org/10.1306/44b4a27b-170a-11d7-8645000102c1865d

Perkins, T., Fox, M., Lee, J., Bernstein, L. S., Berk, A., Matthew, M. W., & Alder-Golden, S. M. (2012). Speed and accuracy improvements in FLAASH atmospheric correction of hyperspectral imagery. *Optical Engineering*, *51*(11), 111707. https://doi.org/10.1117/1.oe.51.11.111707

Portelinha, F. H. M., Lima, D. C., Fontes, M. P. F., & Carvalho, C. A. B. (2012). Modification of a lateritic soil with lime and cement: an economical alternative for flexible pavement layers. *Soils and Rocks, São Paulo*, *35*(1), 51-63.

Pour, A. B., & Hashim, M. (2011). Identification of hydrothermal alteration minerals for exploring of porphyry copper deposit using Aster data, Se Iran. *Journal of Asian Earth Sciences*, *42*(6), 1309–1323. https://doi.org/10.1016/j.jseaes.2011.07.017

Raynolds, R. G., & Johnson, G. D. (1985). Rate of neogene depositional and deformational processes, north-west himalayan foredeep margin, Pakistan. *Geological Society, London, Memoirs*, *10*(1), 297–311. https://doi.org/10.1144/gsl.mem.1985.010.01.24

Reed, F.R.C., 1942, Non-marine lamellibranchs, etc., from the Speckled Sandstone Formation (Punjabian) of the Salt Range: Records of the Geological Survey of India, v. 74, pt. 4, p. 474–492.

Reed, F.R.C., Cotter, G. de P., and Lahiri, H.M., 1930, The Permo-Carboniferous secession in the Warchha valley, western Salt Range, Punjab: Records of the Geological Survey of India, v. 62, pt. 4, p. 412–443.

Retallack, G.J., 1989, Laboratory exercises in paleopedology: Eugene, University of Oregon, 74 p.

Richards, J. A. (1999). *Remote sensing digital image analysis* (Vol. 3, pp. 10-38). Berlin: springer.

Rigassi, V. (1995). Compressed earth blocks: a publication of Deutsches Zentrum für Entwicklungstechnologien—GATE, a division of the Deutsche Gesellschaft für Technische Zusammenarbeit (GTZ) GmbH in coordination with the building advisory service and information network. *Vieweg, Braunschweig*.

Rowan, L. C., Goetz, A. F., & Ashley, R. P. (1977). Discrimination of hydrothermally altered and unaltered rocks in visible and near infrared multispectral images. *GEOPHYSICS*, *42*(3), 522–535. https://doi.org/10.1190/1.1440723

Ryerson, R. A., & Rencz, A. N. (1998). *Manual of Remote Sensing. Remote Sensing for the Earth Sciences* (Vol. 3). John Wiley & Sons.

Sabins, F. F. (1999). Remote Sensing for mineral exploration. *Ore Geology Reviews*, *14*(3-4), 157–183. https://doi.org/10.1016/s0169-1368(99)00007-4

Saing, Z., Samang, L., Harianto, T., & Patanduk, J. (2017). Mechanical characteristic of ferro laterite soil with cement stabilization as a subgrade material. *International Journal of Civil Engineering and ology (IJCIET)*, *8*(3), 609-616.

Schindewolf, O.H., 1964, Über die jungpaläozoische versisung der Salt Range (W. Pakistan): Neues Jahrbuch für Mineralogie, Geologie, und Paleontologie, ser. B, v. 121, no. 1, p. 55–66.

Shah, S.M.I., 1980, Stratigraphy and economic geology of central Salt Range: Records of the Geological Survey of Pakistan, v. 52, 104 p.

Sheffield, C. (1985). Selecting Band Combinations from Multi Spectral Data. *Photogrammetric Engineering and Remote Sensing*, *58*(6), 681-687.

Solutions, H. G., Solutions, E., Learning, E. D., & SARscape, E. N. V. I. (2013). Vegetation analysis: using vegetation indices in ENVI. *Harris Geospational Solutions,[Online]. Available:*

https://www.harrisgeospatial.com/Learn/Whitepapers/TabId/2359/ArtMID/10212/ArticleID/16162/Vegetation-Analysis-Using-Vegetation-Indices-in-ENVI. aspx.

Staub, J. R., & Ferm, J. C. (1979). Estuarine-coastal plain coal deposition in southern West Virginia; Pennyslvanian Beckley Seam. *AAPG Bulletin*, *63*. https://doi.org/10.1306/2f917ff5-16ce-11d7-8645000102c1865d

Talabi, A.O., Obasi R.O., Oyinloye A.O., Ademilua O.L., Adebayo O.F., Olaolorun O.A and Eluwole A.B (2018). Evaluation of Major and Trace Elements of Orin Ekiti Bauxite Clay. Research Journal of Applied Sciences 13 (5): 306-312.

Testa, F., Villanueva, C., Cooke, D., & Zhang, L. (2018). Lithological and hydrothermal alteration mapping of epithermal, porphyry and tourmaline breccia districts in the Argentine andes using Aster imagery. *Remote Sensing*, *10*(2), 203. https://doi.org/10.3390/rs10020203

Thagesen, B. (1996). Tropical Rocks and soils. *Highway and Traffic Engineering in Developing Countries*. https://doi.org/10.4324/9780203223673_chapter_13

The role of Mineral Resources in today's world. EUMICON. (2018, February 23). Retrieved January 10, 2022, from https://www.eumicon.com/en/topics/the-role-of-mineral-resources-in-today-s-world/

Vainer, S., Matmon, A., Erel, Y., Hidy, A. J., Crouvi, O., De Wit, M., Geller, Y., & ASTER Team. (2020). Landscape responses to intraplate deformation in the Kalahari constrained by sediment provenance and chronology in the Okavango Basin. *Basin Research*, *33*(2), 1170–1193. https://doi.org/10.1111/bre.12509

Vogley, A W. (1985). Economics of the Mineral Industries, American Institute of Mining, Metallurgical and Petroleum Engineers, Inc., New York, USA.

Wardlaw, R. B., Martin, W. E., & Iqbal, H. H. (2007). Stratigraphic analysis of Paleocene and Lower Eocene rocks adjacent to the Potwar Plateau, northern Pakistan. *Regional Studies of the Potwar Plateau Area, Northern Pakistan. Bulletin of the US Geological Survey*, 1-18.

Warwick, P. D., & Shakoor, T. (1993). Lithofacies and depositional environments of the coal-bearing Paleocene Patala Formation, Salt Range coal field, northern Pakistan. *Geological Survey of Pakistan, Project Report (IR) PK-109.5, 52*.

Warwick, P.D., and Shakoor, T. (1988), Preliminary report on the coal characteristics in the Salt Range area of north-central Pakistan: U.S. Geological Survey Open-File Report 88–637, 333 p. https://doi.org/10.3133/ofr88637

Weymouth, J. W. (1986). Geophysical methods of archaeological site surveying. *Advances in Archaeological Method and Theory*, 311–395. https://doi.org/10.1016/b978-0-12-003109-2.50010-6

Whitney, C. G., Abbas, S. Q., & Esposito, K. J. (1990). Mineralogy and thermal properties of clay deposits in the salt range and Kala Chitta Range, Punjab Province, Pakistan. *Open-File Report*. https://doi.org/10.3133/ofr90657

Wynne, A.B., 1881, Travelled blocks of the Punjab: Records of the Geological Survey of India, v. 14, pt. 1, p. 153–154.

Yamaguchi, Y., & Naito, C. (2003). Spectral indices for lithologic discrimination and mapping by using the Aster Swir Bands. *International Journal of Remote Sensing*, *24*(22), 4311–4323. https://doi.org/10.1080/01431160110070320

Yeats, R. S., Khan, S. H., & Akhtar, M. (1984). Late quaternary deformation of the Salt Range of Pakistan. *Geological Society of America Bulletin*, *95*(8), 958. https://doi.org/10.1130/0016-7606(1984)95<958:lqdots>2.0.co;2

Young, A., & Goudie, A. (1973). Duricrusts in tropical and subtropical landscapes. *The Geographical Journal*, *139*(3), 545. https://doi.org/10.2307/1795059

Appendix

Table 6 Reduced set of acquired magnetic data from field of study area.

S.no	Station no	UTM-E	UTM-N	Time	Field reading	Anomaly
1	AE10	310824	3619763	11:58:00	50102.3	11
2	AE11	310924	3619763	12:01:00	50115.4	24
3	AE12	311024	3619763	12:04:00	50105.6	14
4	AE13	311124	3619763	12:06:00	50127.3	35
5	AE14	311224	3619763	12:11:00	50108.5	16
6	AE15	311324	3619763	12:14:00	50099.2	7
7	AE16	311424	3619763	12:17:00	50104.8	13
8	AE17	311524	3619763	12:29:00	50062.3	-30
9	AE18	311624	3619763	12:36:00	50182.2	89
10	AE19	311724	3619763	12:41:00	50107.2	14
11	AE20	311824	3619763	12:44:00	50132.5	39
12	AE21	311924	3619763	13:21:00	50077.7	-17
13	AE22	312024	3619763	13:29:00	50137	42
14	AE23	312124	3619763	13:31:00	50117.1	22
15	AE24	312224	3619763	13:34:00	50110.5	16
16	AD24	312224	3619663	13:39:00	50111.3	17
17	AD23	312124	3619663	13:42:00	50108.9	14
18	AD22	312024	3619663	13:46:00	50128.4	33
19	AD21	311924	3619663	13:49:00	50105.8	11
20	AC21	311924	3619563	13:54:00	50122.9	28
21	AC22	312024	3619563	13:59:00	50107.3	12
22	AC23	312124	3619563	14:02:00	50119.6	25
23	AC24	312224	3619563	14:05:00	50113.2	18
24	AB24	312224	3619463	14:11:00	50116.5	22
25	AB23	312124	3619463	14:15:00	50118.2	23
26	AB22	312024	3619463	14:19:00	50119.7	24
27	AB21	311924	3619463	14:23:00	50119.3	24
28	AB20	311824	3619463	14:26:00	50118	23
29	AB19	311724	3619463	14:34:00	50127.5	32
30	AB17	311524	3619463	14:41:00	50142.2	46
31	AB16	311424	3619463	14:43:00	50114	18
32	AC17	311524	3619563	14:49:00	50113.2	16
33	AC16	311424	3619563	14:56:00	50121.8	25
34	AB15	311324	3619463	15:14:00	50109.2	12

35	AB14	311224	3619463	15:27:00	50121.4	24
36	AB13	311124	3619463	15:30:00	50121.6	24
37	AB12	311024	3619463	15:31:00	50090.9	-7
38	AB11	310924	3619463	15:36:00	49973.8	-124
39	AB10	310824	3619463	15:42:00	50116	18
40	AB9	310724	3619463	15:46:00	50119.9	22
41	AC9	310724	3619563	15:49:00	50114	15
42	AC10	310824	3619563	15:53:00	50114.2	15
43	AC11	310924	3619563	16:13:00	50104.2	5
44	AC12	311024	3619563	16:15:00	49954.2	-145
45	AC13	311124	3619563	16:20:00	49950.7	-149
46	AC14	311224	3619563	16:24:00	50114.9	15
47	AC15	311324	3619563	16:32:00	50118.8	19
48	AD16	311424	3619663	16:38:00	50094.6	-6
49	AD15	311324	3619663	16:42:00	50116.4	15
50	AD14	311224	3619663	16:45:00	50193.9	93
51	AD13	311124	3619663	16:49:00	50117.3	16
52	AD12	311024	3619663	16:54:00	50114.2	13
53	AD11	310924	3619663	16:56:00	50121.8	20
54	AD10	310824	3619663	17:02:00	50106.9	5
55	AA8	310624	3619363	8:55:00	50116.1	13
56	AA9	310724	3619363	8:56:00	50116.3	13
57	AA10	310824	3619363	8:58:00	50113	10
58	AA11	310924	3619363	9:06:00	50105.8	3
59	AA12	311024	3619363	9:08:00	50271.8	169
60	AA13	311124	3619363	9:16:00	50114.2	11
61	AA14	311224	3619363	9:20:00	50132.3	29
62	Z14	311224	3619263	9:32:00	50103.2	0
63	Z15	311324	3619263	9:36:00	50116.7	14
64	Z13	311124	3619263	9:39:00	50115.7	13
65	Z12	311024	3619263	9:44:00	50094.1	-9
66	Z10	310824	3619263	9:49:00	50096.8	-6
67	Z9	310724	3619263	9:58:00	50105.2	2
68	Z8	310624	3619263	10:00:00	50106	3
69	Z7	310524	3619263	10:10:00	50106.8	4
70	Y6	310424	3619163	10:17:00	50108.2	6
71	Y7	310524	3619163	10:20:00	50108.4	6
72	Y8	310624	3619163	10:24:00	50117.7	15
73	Y9	310724	3619163	10:27:00	50132.3	30

74	Y10	310824	3619163	10:30:00	50106.9	4
75	Y11	310924	3619163	10:36:00	50118.3	16
76	Y12	311024	3619163	10:39:00	50117.1	15
77	Y13	311124	3619163	10:42:00	50108	5
78	Y14	311224	3619163	10:46:00	50257.5	155
79	Y15	311324	3619163	10:50:00	50107.7	5
80	X15	311324	3619063	10:57:00	50108.9	7
81	X14	311224	3619063	11:00:00	50112.8	11
82	X13	311124	3619063	11:03:00	50113.1	11
83	X12	311024	3619063	11:06:00	50120	18
84	X11	310924	3619063	11:09:00	50119.5	17
85	X10	310824	3619036	11:10:00	50111	9
86	X9	310724	3619063	11:15:00	50055.4	-47
87	X8	310624	3619063	11:21:00	50108	6
88	X7	310524	3619063	11:32:00	50126	24
89	X6	310424	3619063	11:41:00	50109.5	7
90	W6	310424	3618963	11:47:00	50129.5	28
91	W7	310524	3618963	11:53:00	50107.2	5
92	W8	310624	3618963	11:56:00	50099	-3
93	W9	310724	3618963	12:03:00	50258.2	156
94	W10	310824	3618963	12:05:00	50113	11
95	W11	310924	3618963	12:19:00	50130	28
96	W12	311024	3618963	12:22:00	50119.5	18
97	V12	311024	3618863	12:28:00	50119.4	18
98	V11	310924	3618863	12:32:00	50122.1	21
99	V10	310824	3618863	12:35:00	50131.8	30
100	V9	310724	3618863	12:44:00	50130.6	29
101	V8	310624	3618863	12:46:00	50134.7	33
102	V7	310524	3618863	12:50:00	50113.5	12
103	V6	310424	3618863	12:52:00	50100.4	-1
104	V5	310324	3618863	12:55:00	50159.9	58
105	V14	311224	3618863	15:21:00	50127.7	26
106	W14	311224	3618963	15:29:00	50125.3	23
107	X17	311524	3619063	15:38:00	50144	41
108	Y18	311624	3619163	15:44:00	50147.1	44
109	Z20	311824	3619263	15:57:00	50122.2	18
110	AA22	312024	3619363	16:04:00	50142.6	38
111	AA23	312124	3619363	16:08:00	50120.4	16
112	Z21	311924	3619263	16:13:00	50124.9	21

113	Z22	312024	3619263	16:16:00	50126.3	22
114	Y22	312024	3619163	16:20:00	50127.8	24
115	Y21	311924	3619163	16:25:00	50130.2	27
116	Y20	311824	3619163	16:26:00	50124.5	21
117	Y19	311724	3619163	16:30:00	50188.4	85
118	X18	311624	3619063	16:32:00	50117.2	14
119	X19	311724	3619063	16:34:00	50106.3	3
120	X20	311824	3619063	16:36:00	50130.3	27
121	X21	311924	3619063	16:39:00	50126.8	24
122	W21	311924	3618963	16:41:00	50130.1	27
123	W20	311824	3618963	16:42:00	50127.9	25
124	W19	311724	3618963	16:44:00	50133.2	31
125	W18	311624	3618963	16:46:00	50121.2	19
126	W17	311524	3618963	16:49:00	50127	24
127	V19	311724	3618863	16:52:00	50122.6	20
128	V18	311624	3618863	16:54:00	50126.8	25
129	V17	311524	3618863	16:59:00	50131.2	29
130	V16	311424	3618863	17:00:00	50130.3	28
131	V15	311324	3618863	17:04:00	50131.8	30
132	U4	310224	3618763	9:16:00	50127.2	24
133	T2	310024	3618663	9:26:00	50129.1	26
134	T3	310124	3618663	9:31:00	50122.6	20
135	T4	310224	3618663	9:34:00	50109.8	7
136	S2	310024	3618563	9:38:00	50129	27
137	S3	310124	3618563	9:41:00	50347.9	246
138	S4	310224	3618563	9:44:00	50122.1	20
139	R4	310224	3618463	9:47:00	50128.3	26
140	R3	310124	3618463	9:49:00	50124.6	23
141	R2	310024	3618463	9:54:00	50084.4	-17
142	Q2	310024	3618363	9:59:00	50119.6	18
143	P1	309924	3618263	10:03:00	50137.1	36
144	P2	310024	3618263	10:05:00	50135.6	35
145	O1	309924	3618163	10:12:00	50035.1	-65
146	O2	310024	3618163	10:19:00	50029.7	-71
147	N1	309924	3618163	10:22:00	50135	34
148	N2	310024	3618163	10:28:00	50153.3	53
149	M2	310024	3617963	10:41:00	50180.2	81
150	M1	309924	3617963	10:45:00	50149	49
151	L5	310324	3617863	11:18:00	50124.7	26

152	L6	310424	3617863	11:44:00	50127.3	28
153	L7	310524	3617863	11:49:00	50133.2	34
154	L8	310624	3617863	11:53:00	50131.2	32
155	L9	310724	3617863	12:00:00	50129.3	30
156	L10	310824	3617863	12:04:00	50125.9	27
157	L11	310924	3617863	12:25:00	50121.9	23
158	M12	311024	3617963	12:33:00	50129.3	30
159	M11	310924	3617963	12:34:00	50130.3	31
160	N10	310824	3618063	12:43:00	50141.2	41
161	N9	310724	3618063	12:48:00	50135.6	36
162	N8	310624	3618063	12:51:00	50130.3	30
163	N7	310524	3618063	12:53:00	50125.9	26
164	N6	310424	3618063	12:58:00	50146.9	47
165	N5	310324	3618063	13:00:00	50156.2	56
166	N4	310224	3618063	13:03:00	50092.7	-7
167	N3	310124	3618063	13:05:00	50145.9	46
168	L18	311624	3617863	15:14:00	50162.9	64
169	L17	311524	3617863	15:16:00	50153.8	55
170	M16	311424	3617963	15:22:00	50140.6	41
171	N16	311424	3618063	15:24:00	50128	28
172	O16	311424	3618163	15:29:00	50133.1	33
173	P16	311424	3618263	15:37:00	50142.9	42
174	Q16	311424	3618363	15:42:00	50129.1	28
175	R16	311424	3618463	15:46:00	50133.6	32
176	S16	311424	3618563	15:49:00	50132	30
177	T16	311424	3618663	15:53:00	50126.6	24
178	U16	311424	3618763	15:56:00	50125	22
179	U15	311324	3618763	16:00:00	50144.4	42
180	T15	311324	3618663	16:07:00	50126.8	25
181	S15	311324	3618563	16:11:00	50130.1	28
182	R15	311324	3618463	16:15:00	50131.6	30
183	Q15	311324	3618363	16:18:00	50139.1	38
184	P15	311324	3618263	16:23:00	50134.9	35
185	O15	311324	3618163	16:26:00	50138.4	38
186	O14	311224	3618163	16:30:00	50130.3	30
187	O13	311124	3618163	16:33:00	50137.3	37
188	O12	311024	3618163	16:38:00	50137.8	38
189	O11	310924	3618163	16:41:00	50135.8	36
190	O10	310824	3618163	16:45:00	50131.6	32

191	O9	310724	3618163	16:48:00	50151.3	51
192	O8	310624	3618163	16:51:00	50134.3	34
193	O7	310524	3618163	16:54:00	50148.1	48
194	O6	310424	3618163	16:56:00	50128.9	29
195	O5	310324	3618163	16:59:00	50149	49
196	N11	310924	3618063	9:39:00	50148.5	38
197	U10	310824	3618763	9:47:00	50139.5	26
198	U11	310924	3618763	9:55:00	50146.5	33
199	U12	311024	3618763	9:59:00	50133.2	20
200	U13	311124	3618763	10:02:00	50144.7	32
201	U14	311224	3618763	10:07:00	50138.2	25
202	U17	311524	3618763	10:11:00	50140.1	27
203	U18	311624	3618763	10:20:00	50138.9	26
204	U19	311724	3618763	10:21:00	50131.2	19
205	U20	311824	3618763	10:29:00	50135.4	23
206	U21	311924	3618763	10:32:00	50143.3	31
207	U22	312024	3618763	10:34:00	50139.5	27
208	U23	312124	3618763	10:37:00	50142.7	31
209	U24	312224	3618763	10:48:00	50132.1	20
210	U25	312324	3618763	10:57:00	50137.7	26
211	U26	312424	3618763	11:02:00	50131.2	20
212	T26	312424	3618663	11:08:00	50138.8	28
213	T25	312324	3618663	11:12:00	50137.7	27
214	T24	312224	3618663	11:26:00	50140.4	30
215	T23	312124	3618663	11:34:00	50136	26
216	T22	312024	3618663	11:49:00	50139.6	30
217	T21	311924	3618663	11:55:00	50139.7	30
218	T20	311824	3618663	12:00:00	50139.5	30
219	T19	311724	3618663	12:02:00	50142	33
220	T18	311624	3618663	12:05:00	50136.7	27
221	T17	311524	3618663	12:08:00	50135.9	27
222	T14	311224	3618663	12:18:00	50132.3	23
223	T13	311124	3618663	12:19:00	50136.2	27
224	T12	311024	3618663	12:25:00	50132.5	24
225	T11	310924	3618663	12:29:00	50150.1	41
226	S11	310924	3618563	12:31:00	50144.5	36
227	S12	311024	3618563	13:01:00	50137	30
228	S13	311124	3618563	13:03:00	50129.1	22
229	S14	311224	3618563	13:05:00	50130.5	23

230	S17	311524	3618563	13:12:00	50132.6	25
231	S18	311624	3618563	13:14:00	50136.4	29
232	S19	311724	3618563	13:18:00	50136	29
233	S20	311824	3618563	13:30:00	50129.4	23
234	S21	311924	3618563	13:37:00	50135.3	29
235	S22	312024	3618563	13:40:00	50137.8	31
236	S23	312124	3618563	13:47:00	50134.5	28
237	S24	312224	3618563	13:56:00	50148.9	43
238	S25	312324	3618563	13:58:00	50145.3	39
239	R25	312324	3618463	14:02:00	50149.6	44
240	Q25	312324	3618363	14:04:00	50154.3	49
241	Q24	312224	3618363	14:06:00	50159.9	55
242	R24	312224	3618463	14:07:00	50150.3	45
243	R23	312124	3618463	14:10:00	50158.2	53
244	Q23	312124	3618363	14:11:00	50153.1	48
245	Q22	312024	3618363	14:14:00	50154	49
246	R22	312024	3618463	14:20:00	50156.9	52
247	R21	311924	3618463	14:31:00	50131.4	27
248	Q21	311924	3618363	14:33:00	50137.3	33
249	Q20	311824	3618363	14:37:00	50131.3	27
250	R20	311824	3618463	14:40:00	50133.2	29
251	R19	311724	3618463	14:45:00	50136.6	32
252	Q19	311724	3618363	14:51:00	50132.1	29
253	Q18	311624	3618363	14:53:00	50133.3	30
254	R18	311624	3618463	14:58:00	50142.8	39
255	Q17	311524	3618363	15:04:00	50139.5	36
256	R17	311524	3618463	15:10:00	50142	39
257	Q14	311324	3618363	15:28:00	50151.3	49
258	R14	311324	3618463	15:32:00	50135.4	33
259	R13	311224	3618463	15:35:00	50131.4	29
260	Q13	311224	3618363	15:38:00	50137	35
261	Q12	311024	3618363	15:40:00	50132.6	30
262	R12	311024	3618463	15:42:00	50133.7	31
263	Q11	310924	3618363	15:45:00	50131.2	29
264	R11	310924	3618463	15:48:00	50141.1	39
265	Q10	310824	3618363	15:53:00	50144.4	43
266	R10	310824	3618463	15:56:00	50147.2	45
267	Q9	310724	3618363	15:58:00	50144.6	43
268	Q8	310624	3618363	16:00:00	50142	40

269	P8	310624	3618263	8:39:00	50135.8	36
270	P9	310724	3618263	8:43:00	50141.9	42
271	P10	310824	3618263	8:46:00	50147.1	47
272	P11	310924	3618263	8:49:00	50139.1	39
273	P12	311024	3618263	8:52:00	50134.5	34
274	P13	311124	3618263	8:55:00	50121.4	21
275	P14	311224	3618263	8:58:00	50145	45
276	P17	311524	3618263	9:15:00	50137.7	37
277	O17	311524	3618163	9:21:00	50124.9	25
278	O18	311624	3618163	9:25:00	50126.9	27
279	P18	311624	3618263	9:27:00	50129.6	29
280	P19	311724	3618263	9:32:00	50120	19
281	O19	311724	3618163	9:34:00	50139.9	40
282	O20	311824	3618163	9:37:00	50134.8	35
283	P20	311824	3618263	9:39:00	50128.5	28
284	O21	311924	3618163	9:47:00	50134.5	34
285	P21	311924	3618263	9:51:00	50131.1	30
286	P22	312024	3618263	9:58:00	50138.3	38
287	O22	312024	3618163	10:02:00	50139.8	40
288	P23	312124	3618263	10:07:00	50123.2	22
289	O23	312124	3618163	10:10:00	50126.8	26
290	N24	312224	3618063	10:50:00	50113.4	13
291	M25	312324	3617963	10:54:00	50127.5	28
292	M24	312224	3617963	10:59:00	50159	59
293	N23	312124	3618063	11:04:00	50156.9	57
294	L25	312324	3617863	11:07:00	50167	68
295	L24	312224	3617863	11:11:00	50153.9	55
296	M23	312124	3617963	11:17:00	50150.4	51
297	M22	312024	3617963	11:21:00	50137.8	38
298	M21	311924	3617963	11:27:00	50147.8	48
299	N20	311824	3618063	11:29:00	50138.8	38
300	N21	311924	3618063	11:31:00	50135.5	35
301	N22	312024	3618063	11:32:00	50126.7	26
302	L23	312124	3617863	11:35:00	50143.6	44
303	L22	312024	3617863	11:37:00	50143.6	44
304	L21	311924	3617863	11:43:00	50163.1	64
305	L20	311824	3617863	11:48:00	50145.8	46
306	M17	311524	3617963	12:25:00	50146.6	46
307	N17	311524	3618063	12:26:00	50148.4	48

308	L16	311424	3617863	12:36:00	50146.2	46
309	L15	311324	3617863	12:42:00	50168.1	68
310	M15	311324	3617963	12:47:00	50135.7	35
311	N15	311324	3618063	13:03:00	50131.4	31
312	N14	311224	3618063	13:07:00	50131.6	31
313	M14	311224	3617963	13:09:00	50128.2	28
314	L14	311224	3617863	13:14:00	50140.1	40
315	L13	311124	3617863	13:18:00	50139	39
316	M13	311124	3617963	13:21:00	50138.5	38
317	N13	311124	3618063	13:24:00	50136.9	36
318	N12	311024	3618063	13:27:00	50139.5	39
319	L12	311024	3617863	13:34:00	50111.6	11
320	M10	310824	3617963	13:44:00	50143.9	43
321	M9	310724	3617963	13:47:00	50142.5	42
322	M8	310624	3617963	13:49:00	50145.2	45
323	M7	310524	3617963	13:53:00	50149.6	49
324	M6	310424	3617963	13:56:00	50145.5	45
325	M5	310324	3617963	13:58:00	50121.8	21